Development of Small Animal PET Detectors based on Multi-Wire Proportional Chambers

Jennifer Bersch

Diplomarbeit

Institut für Kernphysik
Mathematisch-Naturwissenschaftliche Fakultät
Westfälische Wilhelms-Universität Münster

Dezember 2011

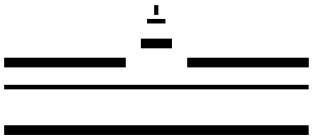

Westfälische
Wilhelms-Universität
Münster

Referent:	Prof. Dr. Johannes P. Wessels
Korreferent:	Prof. Dr. Alfons Khoukaz

Dans la vie, rien n'est à craindre, tout est à comprendre.

— Marie Curie —

Contents

I Introduction

Positron Emission Tomography (PET) is an imaging method with increasing importance in everyday nuclear medicine. It is called *emission tomography* because there are two underlying principles. There is at first the *tracer principle*, which includes imaging by using gamma-ray emission. Second, there is the *tomography principle*, which means volumetric imaging of the body's interior.

Due to these principles, PET is able to visualize metabolic processes within living organisms. Consequently, PET has been successful in correlation with detection of tumors, myocardial diseases, and identification of diseased brain regions. Actual research projects are especially oncological, cardiological, and neurological studies. These studies often start on the pre-clinical level using Small Animal PET devices for research purposes. Due to the small organism of mice or rats, the PET devices should possess a high spatial resolution. Additionally, the sensitivity regarding photon detections is a major factor when evaluating a PET device.

Traditional PET devices are scintillator based. Common Small Animal PET scanners have a spatial resolution of about 1 mm and above. Restricted by the involved physics processes, the maximal possible resolution is only little below this.

A promising alternative to the traditional device is a PET scanner based on the principle of Multi-Wire Proportional Chambers (MWPC). Invented in the 1970s, it was sold by Oxford Positron Systems. Today the company is not in business anymore and the existence of such scanners is very rare. The problem has been the more complex operation and maintenance of these PET devices in comparison to scintillation based scanners. However, the possibility of reaching higher spatial resolution and the lower costs of production make it still very attractive.

Two MWPC-based PET scanners (quadHIDACs) are currently in use at the European

Institute for Molecular Imaging Muenster providing satisfying research results, but the lack of support and service of the quadHIDAC makes operation difficult. A project (B6) has been launched to develop a high-resolution Small Animal PET based on MWPCs hosted by the Sonderforschungsbereich 656 "Molecular Cardiovascular Imaging". This project currently focuses on two main aspects. On the one hand, there is the development of a new technique to optimize and manufacture photon-electron converters. On the other hand, there is a strong interest in repairing old quadHIDAC modules for further improved operation of the quadHIDAC scanner.

Considering this context, this thesis focuses on three main parts: the implementation of Geant4 simulations to examine the predictions for the sensitivity of the quadHIDAC by optimizing the converter geometry (chapter VI), the development of a read out for quadHIDAC modules outside of the scanner environment (chapter VII), and the design and setup of a converter test device to evaluate the operation of built prototype converters (chapter VIII).

II

Physics Background

As positron emission tomography is a nuclear imaging method, radioactive decay plays an important role. Before a PET scan is carried out, a radioactively marked molecule, called tracer, is injected to the patient. The molecule decays inside the patient and photons leaving the body are detected. In relation to this aspect, this chapter gives a short overview on the physical background of radioactive decay and the interaction of radiation with matter.

II.1. Radioactive decay

There are three kinds of radioactive processes named α, β, and γ- decay, which originate from the atomic nucleus. Speaking of α- decay, the parent nuclear nucleus (preferably holding a high atomic number Z) emits a Helium nucleus ($^4He^{2+}$). This nucleus is relatively heavy depositing high amounts of energy in small volumes. Due to the large cross section, Helium nuclei are likely to interact with matter and therefore relatively easy to shield.
β- particles are either high energetic electrons or positrons. Their emission is one type of ionizing radiation. Compared to a Helium nuclei, their cross section is much smaller, which makes shielding more complicated.
γ- radiation is electromagnetic radiation initiated by transitions between different energy levels of an atomic nucleus. It appears usually in correlation with α- or β- decay. Whereas α- and γ- radiation is mono-energetic, the spectrum of β- decays is continuous. At first, this fact seemed to violate the conservation of momentum, but later, it lead to the assumption that β- decay is not a two-body decay. Solving the problem, *Wolfgang Pauli* postulated 1930 the existence of a third generated particle of spin 1/2 (the

neutrino). It was detected in 1956 by *Cowan* and *Reines* [Cow56], but its mass has not been exactly determined and is still in the focus of research projects.
Today the β- decay is explained as a three-body decay grouped into three classes:

- β^-- decay:

$$n \longrightarrow p + e^- + \bar{\nu}_e + Q(\beta^-) \tag{II.1}$$

  This process is the decay of a neutron n into a proton p, an electron e^-, and an electron-anti-neutrino $\bar{\nu}_e$. This decay is even possible for free neutrons because the Q- value[1] of this reaction is greater than zero.

- β^+- decay:

$$p \longrightarrow n + e^+ + \nu_e + Q(\beta^+) \tag{II.2}$$

  The process of a proton decaying into a neutron, a positron, and an electron-neutrino is restricted to the nucleus only. It is not possible for free protons because of the higher mass of the neutron compared to the proton, which results in a negative Q- value.

- electron capture:

$$p + e^- \longrightarrow n + \nu_e + Q(EC) \tag{II.3}$$

  In this case, a proton of the nucleus captures an electron of the atomic shell, usually originated from the K-shell, arising a neutron and a neutrino. This is the second possibility of creating a positron competing with the β^+- decay [Bet08]. Regarding the Q- values, one obtains $Q(EC) = Q(\beta^+) + 2m_e$. This explains why electron capture is energetically favored. Since the Q- value for free protons $Q(EC)_p$ is smaller than zero, the hydrogen atom cannot decay, which assures existence [Leo87].

II.2. Interaction of radiation with matter

The detection principle is based on the interaction between particles and electromagnetic radiation with matter. The behavior of photons and charged particles in matter is very different. Whereas charged particles lose their energy due to their charge, mainly via multiple inelastic collisions with atomic electrons, the interaction of photons with

[1] The Q- value indicates the available energy of the reaction split between the generated particles as their kinetic energy.

matter consists of absorption and scattering. There are three main effect: the photoelectric effect, the Compton effect, and pair production with cross sections depending on the incident energy of the photon [Leo87].

II.2.1. Photons

The penetration of matter by photons is described by the *Beer–Lambert law* given in equation II.4. The number of photons penetrating an absorber decreases exponentially. With I_0 indicating the intensity of the incident beam and the absorption coefficient μ, the intensity I at the position x is then given by

$$I(x) = I_0\, e^{-\mu x}. \tag{II.4}$$

The absorption coefficient depends on the electron density of the absorber material and the photon energy.

Photoelectric effect

The photoelectric effect is the process of a photon being absorbed by an atom ejecting an electron as shown in figure II.1.

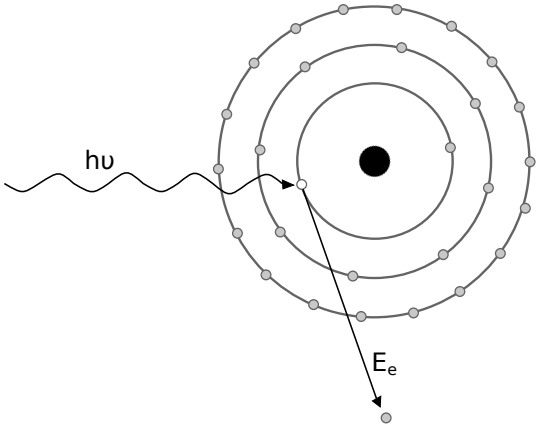

Figure II.1.: *Photoelectric effect [Tow06].*

This process of interaction usually occurs between photons and electrons of inner shells. Consequently, more loosely bound outer shell electrons can fill the inner shell leading to the emission of X-rays. Alternatively, a second electron can be emitted removing the excess energy. This electron is then called *Auger* electron. The recoil energy of this process (typically some eV) is absorbed by the entire atom.

The photoelectric effect dominates for rather low photon energies up to approximately 100 keV.
The ejected electron will have an energy of

$$E_e = h\nu - E_B \tag{II.5}$$

with Planck's constant h, the frequency of the photon ν, and the binding energy of the electron E_B. The binding energy depends on the shell (K-, L-, M- shell), the electron is ejected from. For photon energies above the energy of the K- shell, K electrons are usually involved.
The cross section of the photoelectric effect in the K- shell can mathematically be described as

$$\sigma_{\text{photo}}(K) = \left(\frac{32}{\epsilon_\gamma^7}\right)^{1/2} \alpha^4 \, Z^5 \, \sigma_{\text{Th}}^e. \tag{II.6}$$

The energy ϵ_γ represents the reduced photon energy $E_\gamma / m_e \, c^2$ and the fine-structure constant α can be approximated by $1/137$.
The Thomson differential cross section σ_{Th}^e for elastic scattering is defined as

$$\sigma_{\text{Th}}^e = \frac{8}{3}\pi r_e^2 \tag{II.7}$$

with the classical radius of an electron r_e. The cross section depends on the atomic number and is proportional to Z^4 or Z^5 at MeV energies. Therefore, high Z materials are often in use when building γ-ray detectors. The much more complicated cross section of the photoelectric effect in the L- and M- shell has been calculated by Davisson [Dav68] [Bet08].
The photoelectric effect is irrelevant for organic material, but plays an important role for PET/CT systems. In this case, the PET data is corrected with an attenuation factor determined by the X-ray CT system [Tow06].

Compton effect

The Compton effect must be taken into account for energies above 100 keV and below ≈ 2 MeV. It describes the scattering of photons on electrons as shown in figure II.2. The excess energy originating from the photon's change of direction is split between the binding energy, in case of a bound electron, and the kinetic energy transmitted to the electron. The binding energy is indeed negligible compared to the incident photon energy. Therefore, there is no difference in calculating the Compton effect for free or bound electrons. The electron is always considered to be free.

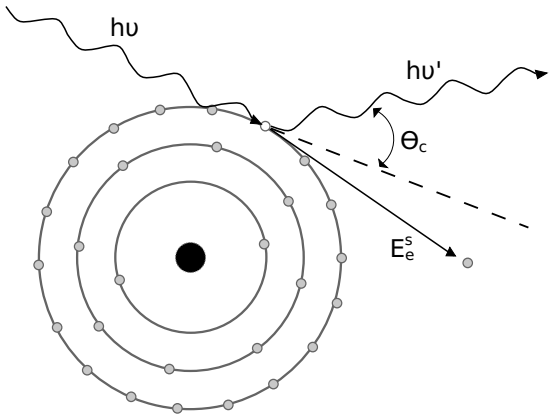

Figure II.2.: *Compton effect [Tow06].*

The energy of the scattered photon can be kinematically derived and is given with respect to figure II.2 by

$$E'_\gamma = h\nu' = \frac{h\nu}{1 + \epsilon_\gamma(1 - \cos\theta_c)} \; . \tag{II.8}$$

The maximum energy loss of the photon occurs at $\theta_c = 180°$. In this case, the photon is *back-scattered* [Tow06].
The total cross section for Compton scattering is

$$\sigma_c = 2\pi r_e^2 \left\{ \frac{1+\epsilon_\gamma}{\epsilon_\gamma^2} \left[\frac{2(1+\epsilon_\gamma)}{1+2\epsilon_\gamma} - \frac{\ln(1+2\epsilon_\gamma)}{\epsilon_\gamma} \right] + \frac{\ln(1+2\epsilon_\gamma)}{2\epsilon_\gamma} - \frac{1+3\epsilon_\gamma}{(1+2\epsilon_\gamma)^2} \right\} \tag{II.9}$$

with the classical electron radius r_e. This was first calculated and noted by *Klein* and *Nishina* in 1929, and is known today as the *Klein-Nishina formula*.
For an atom with atomic number Z, the cross section is given by

$$\sigma_c^Z = \mathrm{Z}\,\sigma_c \; . \tag{II.10}$$

Based on the Klein-Nishina formula, the total cross section can be separated in scattering and absorption cross section giving the fraction of the photon energy transferred to the electron. The scattering cross section is defined as

$$\sigma_c^s = \frac{E'_\gamma}{E_\gamma}\sigma_c \tag{II.11}$$

and therefore the absorption cross section is defined as

$$\sigma_c^a = \sigma_c - \sigma_c^s \; . \tag{II.12}$$

The maximum energy $E^e_{\max}$ transferred to the recoil electron is known as the *Compton edge* [Bet08].

$$E^e_{\max} = h\nu \left(\frac{2\epsilon_\gamma}{1 + 2\epsilon_\gamma} \right) \tag{II.13}$$

Pair production

Pair production occurs for photon energies above 1.022 MeV. The photon passing the Coulomb field of a nucleus transforms into an electron-positron pair. The probability for pair production rises with the incident photon energy. Any energy above 1.022 MeV will be distributed between the kinetic energies of electron and positron and the recoiling nucleus. However, pair production is not of relevance for PET-detectors due to its energy interval.

A summarizing diagram on the relation between incident photon energy and absorption coefficient is shown in figure II.3 using the example of lead. The total absorption coefficient $\mu = 1/\sigma$ is given by the sum of the single fractions.

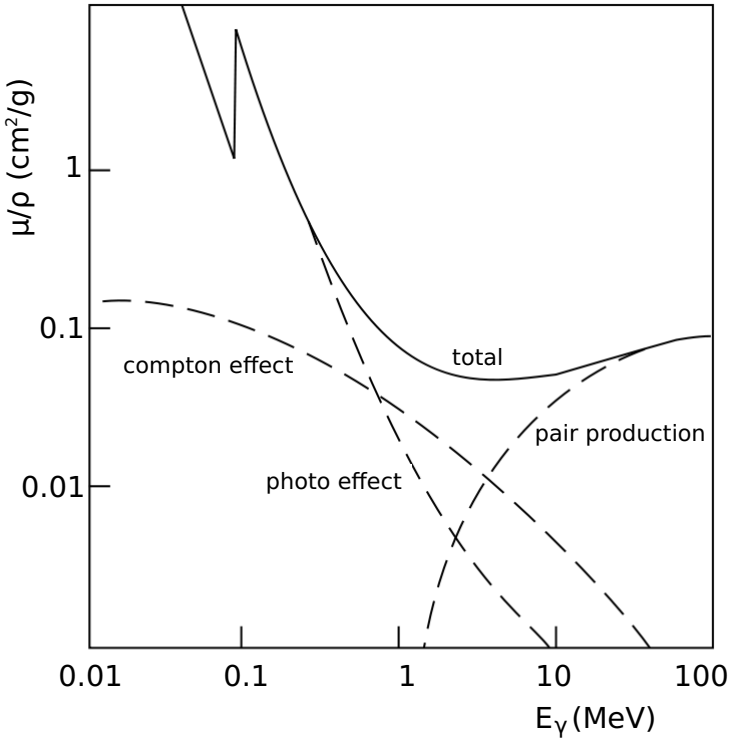

Figure II.3.: *Dependence of the absorption coefficient on the incident photon energy in lead [Pov04].*

II.2.2. Charged particles

The interaction of charged particles with matter consists of the Coulomb interaction of the particles with the atomic electrons. The interaction process results in a loss of energy of the particles as well as in elastic scattering with the atomic nuclei. This deflects the particles from their initial direction. However, the inelastic collisions, which cause ionization and excitation of the surrounding atoms, greatly dominate, and a first approximation of the stopping power neglects elastic scattering for particles heavier than electrons. The energy transferred per inelastic collision is very small, but because there are a high number of collisions per unit length, it results in a substantial energy loss.

The average energy loss per unit length dE/dx was quantum-mechanically first calculated by *Bethe* and *Bloch*. *The Bethe-Bloch-formula* containing density effect correction δ and shell correction C is defined as [Leo87]:

$$-\frac{dE}{dx} = 2\pi N_a r_e^2 m_e c^2 \, \rho \frac{Z}{A} \frac{z^2}{\beta^2} \left[\ln \left(\frac{2m_e \gamma^2 v^2 E_{\max}}{I^2} \right) - 2\beta^2 - \delta - 2\frac{C}{Z} \right] \tag{II.14}$$

with

r_e :	classical electron radius	ρ:	density of absorbing material
m_e:	electron mass	z:	charge of incident particle in units of e
N_a:	Avogadro constant	β=	v/c of the incident particle
Z:	atomic number of	γ=	$1/\sqrt{1-\beta^2}$
	absorbing material	$E_{\max}$:	energy of knock-on collision
A:	atomic weight of	I:	mean excitation potential
	absorbing material		

The density effect correction is important for higher incident particle energies. It is caused by the electric field of the particle, which polarizes atoms along its way shielding the particle's full electric field. As this effect depends on the density of the material and is obviously more pronounced in condensed material than in gases, it is called density effect.

The shell effect occurs when the particle's velocity is smaller than the orbital velocity of the bound electrons, and the approximation of the electron being stationary becomes invalid.

Describing the stopping power of electrons or positrons, the Bethe-Bloch formula must be varied considering the deflection of the low mass particles from their initial path and

a relativistic calculation for fast particles.

$$-\frac{dE}{dx} = 2\pi N_a r_e^2 m_e c^2 \, \rho \frac{Z}{A} \frac{1}{\beta^2} \left[\ln \frac{\tau^2(\tau+2)}{2(I/m_e c^2)^2} + F(\tau) - \delta - 2\frac{C}{Z} \right] \tag{II.15}$$

The energy τ represents the reduced kinetic energy of the particle. The formula $F(\tau)$ differs for the differently charged particles in the following way [Leo87]:

$$F^{e^-}(\tau) = 1 - \beta^2 + \frac{\tau^2/8 - (2r_e + 1)\ln 2}{(\tau+1)^2} \, , \tag{II.16}$$

$$F^{e^+}(\tau) = 2\ln 2 - \frac{\beta^2}{12}\left(23 + \frac{14}{(\tau+2)^2} + \frac{4}{(\tau+2)^3}\right) \, . \tag{II.17}$$

III

Positron Emission Tomography

In chapter II, the most important basics related to positron emission tomography have been explained. This chapter deals with the importance of tracer and the physical processes which are relevant when working with PET. It outlines the complexity of radionuclides, the detection principle based on annihilation, and the different types of events which occur during detection processes.

III.1. Tracer

A radioactively labeled molecule, which is inserted into the object to be examined, is called tracer. The tracer principle was already proposed in the early 1900s by George de Hevesy, who received the Nobel Prize in Chemistry in 1943. It is based on the fact that radioactive isotopes behave in an organism's physiological processes just the same as the stable isotope. With the help of a tracer, PET makes it possible to visualize among others glucose metabolism, blood flow, and receptor density [Wer04].
Before a PET examination, the patient or animal has to be prepared which means that the liquefied tracer is injected to the vein of a patient. This can either happen a set time period before a scan or directly during a scan depending on the isotope. A PET scan of a human takes around 40 minutes. To avoid artifacts, it is very important that the patient stays calm during this period. When animals are involved in the process, they are usually given anesthetics.
Research on tracers has been very intense in the past years. Consequently, a large variety of them exists. For humans and animals, it is important to keep radiation exposure at a minimum, therefore radionuclides used for these purposes should preferably have short half lives. The chart in table III.1 shows several radionuclides used for PET, their

half life, and maximum energy.

The main tracer molecule in today's applications is ^{18}F-fluorodeoxyglucose (^{18}F-FDG) built up of the two constituents FDG, an analog of glucose, and ^{18}F, the radioactive label. ^{18}F-FDG is able to visualize local glucose uptakes of the body. It has an acceptable half life and is chemically comparatively easy to handle. When created, an OH-group is substituted by a ^{18}F-atom as seen in figure III.1. ^{18}F-FDG has been used to detect malignant tumors, which appear very bright on a PET-image compared to the relatively dark background tissue. It is also in practice if there is interest in neuronal activations.

Table III.1.: *List of radionuclides with β^+- decay significant to PET [Bet08].*

Radionuclide	Half-life		$E_{\max}$(MeV)
^{11}C	20.4	min	0.96
^{13}N	9.97	min	1.20
^{15}O	122	s	1.73
^{18}F	109.8	min	0.63
^{22}Na	2.60	y	0.55
^{62}Cu	9.74	min	2.93
^{64}Cu	12.7	h	0.65
^{68}Ga	67.6	min	1.89
^{76}Br	16.2	h	various
^{82}Rb	1.27	min	2.60, 3.38
^{124}I	4.17	d	1.53, 2.14

Furthermore, there are other rather popular molecules marked with ^{18}F such as ^{18}F-fluorodihydroxyphenylalanine (^{18}F-DOPA), a neurotransmitter and analog of dopamine, or ^{18}F-choline used in prostate cancer diagnosis. Besides ^{18}F, which is used routinely in hospitals nowadays, ^{11}C is the second isotope more common. The most part of available radionuclides is generally restricted for research purposes.

III.2. Annihilation

The β^+- decay, as mentioned in section II.1, is the emission of a positron carrying a certain amount of kinetic energy, which is rapidly lost via inelastic scattering in electron-rich environments. Having reached approximately the kinetic energy of a bound elec-

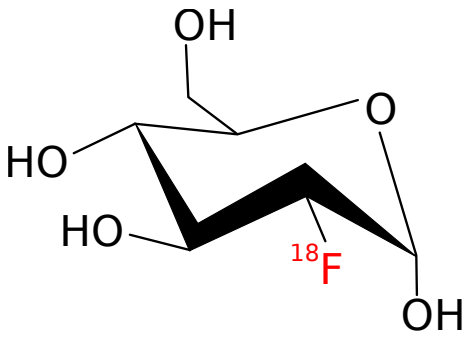

Figure III.1.: ^{18}*F-Fluorodeoxyglucose (FDG) with the position of substitution marked in red.*

tron, the electron and the positron will form a hydrogen-like state called *positronium*. The positronium is unstable and will decay within 10^{-10} s.
The released amount of energy E_{release} can be calculated kinematically, assuming that electron and positron are nearly at rest, with the mass of the electron m_{e^-} and the mass of the positron m_{e^+}.

$$E_{\text{release}} = m_{e^-}c^2 + m_{e^+}c^2 = 1.022\,\text{MeV} \tag{III.1}$$

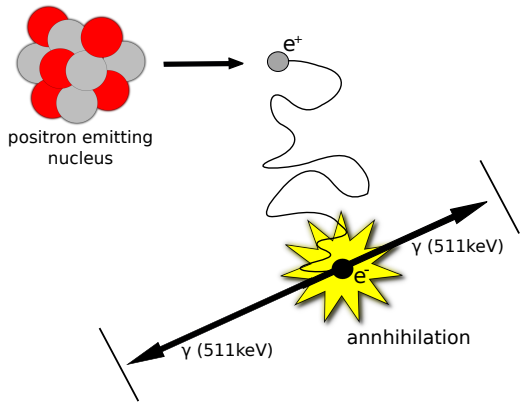

Figure III.2.: *Annihilation process resulting in two 511 keV photons.*

This energy will usually be released in an annihilation creating two 511 keV photons (see figure III.2) in opposite directions (180° angle), thus conserving net momentum, which is nearly zero. Higher orders of annihilation, creating three or more photons, are possible, but very unlikely with a probability smaller than 1 % [Phe06] [Tow06].
Due to the high photon energies, they are able to escape the body retaining a geometrical correlation. The process of detection makes use of this geometrical relationship. If two

detectors receive a photon signal within a set time interval of 2τ[1], a coincidence is recorded and the *line of response* (LOR) between the detectors is calculated. The LOR indicates the location of the annihilation process and therefore the approximate location of the positron emission.

III.3. Coincidences

So far, the location of the annihilation process has been determined up to a straight line. There are two possibilities of identifying the exact position.
One attempt is to measure the difference in arrival time of the photon signals at the detectors. However, the implementation of this method known as *time of flight* is difficult and expensive. The reason for that is the high time resolution which is necessary to receive the required spatial resolution.
The common identification method involves *computed tomography*. The circular geometry of a PET- detector allows the detection of events from many angles. In a typical PET examination, millions of coincidences, originating from a positron-emitting source, are detected. The concentration of the positron-emitting source in the body can then be calculated with the help of mathematical algorithms.
Speaking of coincidences, there are two phenomena shown in figure III.3 which influence the determination of the LOR. These phenomena specify the limit of spatial resolution which is maximally obtained with a PET- detector.

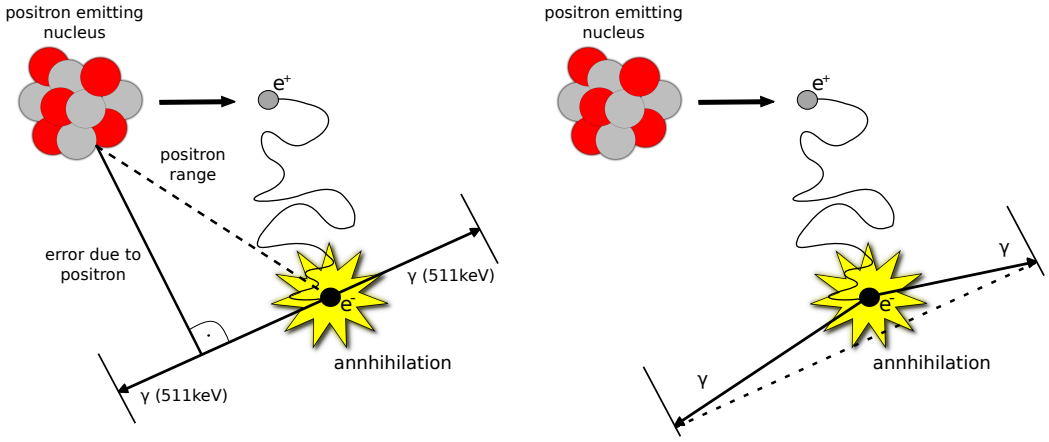

Figure III.3.: *Phenomena which appear when determining the position of the β-decay: positron range (left) and noncolinearity (right).*

[1] τ: electronic coincidence time window

The first effect is caused by the positron range. The position of the emission of the positron is not identical with the position of the annihilation. Consequently, the LOR does not represent the line on which the nucleus decays. The positron's path in the body is determined by multiple interactions changing the positron's direction several times. Therefore, the path is considerably longer than the actual difference between LOR and decaying nucleus. The positron range effect is radionuclide-dependent because of the differences in energy of the emitted positrons.
The second effect is caused by the fact that at the time of annihilation, electron and positron are not fully at rest. This results in a net momentum differing from zero which induces a back-to-back scattering at an angle slightly smaller than 180°. This effect is known as *noncolinearity*. The noncolinearity effect is radionuclide-independent [Phe06].

III.4. Types of events

In a PET scanner, there are four types of coincident events which can be detected. They are shown in figure III.4.

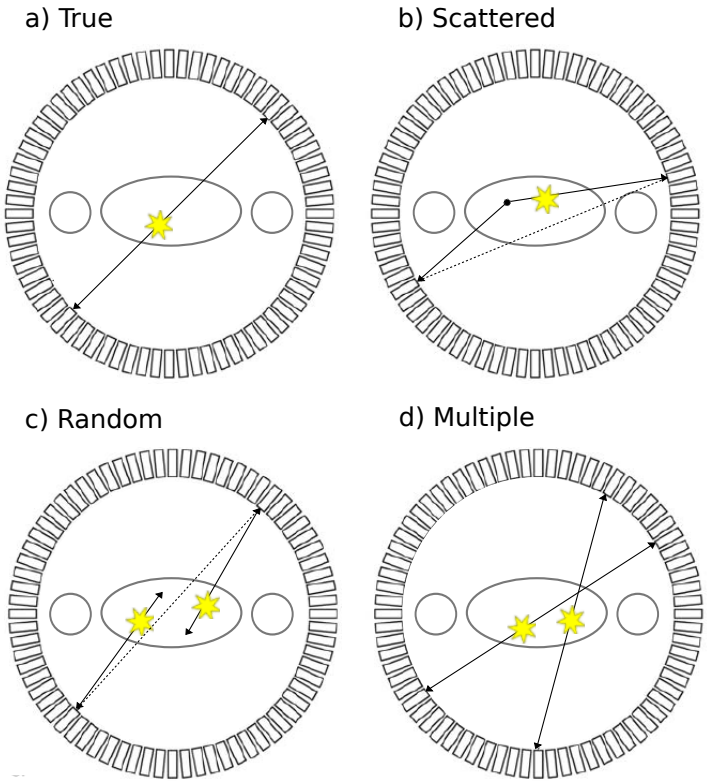

Figure III.4.: *Four types of events in a PET scanner [Phe06].*

The detected coincidences are a mixture of *true*, *scattered*, *random*, and *multiple* coincidences. The event of true coincidence has already been discussed earlier (see section III.2).

In a scattered coincidence one of the two photons originating from the same annihilation interacts with its surrounding matter and changes direction. Since the energy loss caused by Compton scattering can be rather small, the photon will still be properly detected, but the calculated LOR will hint to a false spatial information as shown in figure III.4 b). Scattered coincidences lead to low spatial frequency background reducing contrast. Unfortunately, the corrections are not easy to implement. The fraction obviously depends on the distribution of radioactivity and the shape of the examined medium and differs from 15 % to over 50 %.

It is important to mark that overall, most of the detected photons are *single* events, in which case one of the two annihilation photons has not been recorded. These single events are responsible for random and multiple coincidences.

As mentioned earlier, a coincidence will be recorded if two photons hit two detectors within a time interval of 2τ. It might then happen that two unrelated photons, originating from two different annihilation processes, hit the detectors within the set time window forming a valid event. This coincidence is known as *random* coincidence (figure III.4 c)). The random coincidences generate a background due to misleading spatial information. If N_1 and N_2 are the individual photon detection rates of a detector pair given in counts per second, the rate of random coincidences N_R will be:

$$N_R = 2\tau\, N_1\, N_2\ . \tag{III.2}$$

Due to the direct proportionality of the rate of random coincidences and the *coincidence time window* τ, it is important to keep the time window as short as possible to avoid unnecessary background.

Considering high count rates, it is possible that more than two detectors are responding within the coincidence time window. This case is called *multiple* coincidence (figure III.4 d)). In this case, the reconstruction of the LOR turns out to be nonspecific. That is the reason why multiple coincidences are disregarded. However, they can still contain spatial information because, considering the response of three detectors, the corresponding events often consist of a true coincidence plus a single from an unrelated event [Phe06].

IV

Basics of Gas Proportional Counting

The Multi-Wire Proportional Chamber (MWPC) is the detector principle which is used in the experimental setup in the laboratory. To understand the process of the development of a signal in a MWPC (chapter V), it is useful to understand the basics of a counter tube first. Therefore, this chapter deals with the basic counter tube regarding its electric field inside and the different modes of operation. Additionally, there will be a closer look on the process of avalanche multiplication and the effects of the filling gases.

IV.1. General operation

A counter tube is a configuration of two coaxial cylinders building a capacitor as shown in figure IV.1. The inner cylinder consists of a thin wire which is held at a potential $+Q$. The outer cylinder is usually grounded. This results in an radial electric field between the two cylinders. The space between the two cylinders of a counter tube is filled with a suitable gas, for instance a noble gas like argon.

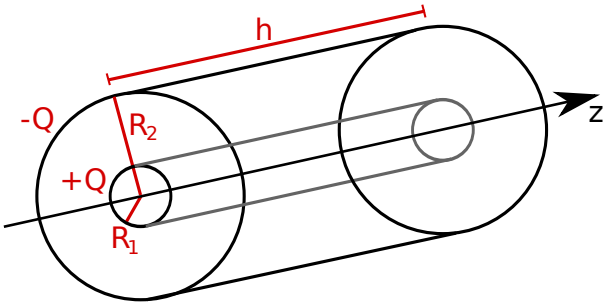

Figure IV.1.: *Coaxial capacitor.*

To obtain the electric field of the capacitor, it is necessary to calculate the flux of the electric field through the surface of an additional coaxial cylinder. Since the electrical field is perpendicular to the surface, the surface element can be written as [Nol89]:

$$d\mathbf{f} = (\rho \; d\phi \; dz) \; \mathbf{e}_\rho \; . \tag{IV.1}$$

By applying cylindrical coordinates $\mathbf{r} = (\rho,\phi,z)$ and by using the Gaussian law, one obtains for the surface integral of the electric field:

$$\int\limits_S \mathbf{E} \; d\mathbf{f} = \rho \; E(\rho) \; 2\pi h = \frac{1}{\varepsilon_0} \int\limits_V \rho(\mathbf{r}')d^3r' = \left\{ \begin{array}{ll} \frac{1}{\varepsilon_0}Q & \text{for } R_1 < \rho < R_2 \\ 0 & \text{else} \end{array} \right\} . \tag{IV.2}$$

The electric field itself is then given by:

$$\mathbf{E}(\mathbf{r}) = \left\{ \begin{array}{ll} \frac{Q}{2\pi\varepsilon_0 h\rho}\mathbf{e}_\rho & \text{for } R_1 < \rho < R_2 \\ 0 & \text{else} \end{array} \right\} . \tag{IV.3}$$

The electric potential for the region of interest for $R_1 < \rho < R_2$ is maintained via integration considering the physical boundary conditions.

$$\phi(\mathbf{r}) = \frac{Q}{2\pi\epsilon_0 h} \ln \frac{R_2}{\rho} \tag{IV.4}$$

This results in a voltage difference of

$$U = \frac{Q}{2\pi\epsilon_0 h} \ln \frac{R_2}{R_1} \; . \tag{IV.5}$$

Applying $Q = CU$, one obtains the capacitance of the cylindrical capacitor.

$$C = \frac{2\pi\epsilon_0 h}{\ln\left(R_2/R_1\right)} \tag{IV.6}$$

When comparing equation IV.3 and IV.5, the relation between electric field and voltage is given by

$$E(\rho) = \frac{U}{\rho \ln\left(R_2/R_1\right)} \; . \tag{IV.7}$$

Considering the case of ions moving towards the tube wall with a velocity $v = \mu E$, with μ being the mobility, and including the condition of $\rho(t = 0) = R_1$, the ions' trajectory is described as [Blu08]:

$$\frac{d\rho(t)}{dt} = \mu \frac{U}{\rho(t) \ln\left(R_2/R_1\right)} \; . \tag{IV.8}$$

From this follows:

$$\rho(t) = R_1 \sqrt{1 + \frac{t}{t_0}} \qquad \text{with} \quad t_0 = \frac{R_1^2 \ln\left(R_2/R_1\right)}{2\mu U} \; . \tag{IV.9}$$

The time t_0 for an electron signal is usually about a few nanoseconds resulting in a quickly fading signal at the anode wires. The ions have a much longer way ($\approx R_2$). The time of the signal is then four to six orders of magnitude larger[1] with a maximal travel time of

$$t_{\max} = t_0 \left[\left(\frac{R_2}{R_1} \right)^2 - 1 \right]. \tag{IV.10}$$

IV.2. Regions of detector operation

A counter tube can be used as *ionization chamber*, *proportional counter* or *Geiger-Mueller counter* depending on the parameters of operation. In the low voltage region, radiation penetrating the tube creates electron-ion pairs, which are accelerated towards the anode and cathode by the electric field. If all created electron-ion pairs are collected and a voltage increase does not show any more effect, the working region of the *ionization chamber* is reached.
If the voltage is then increased further, the strength of the electric field will accelerate primary electrons up to an energy at which they are able to create secondary electron-ion pairs. This way an avalanche of electrons is created close to a wire. The measured current is now directly proportional to the number of primary electrons. A detector operating under these circumstances is called *proportional chamber*.
If the voltage is increased beyond the region of the proportional chamber, the region of limited proportionality is reached. In this region, the amount of created electron-ion pairs deforms the electric field at the anode. If the voltage is raised further, discharges will occur in the gas. To stop the discharge, a quenching gas must be added. This is the region a *Geiger-Mueller* counter works at. In figure IV.2, the typical plateau of stable heights of pulses can be seen.
Any further increase of voltage brings along a continuous breakdown, which is to be avoided to prevent permanent damage [Leo87].

IV.3. Townsend avalanche

Since the electric field is strongest at the anode wires decreasing with $1/\rho$ towards the cathode, electrons near the cathode will be drifting towards the wires. Only at very short distances, when the electric field reaches extremely high values due to the thin wire geometry, electrons gain enough energy to cause avalanches. The basis of

[1] a typical value lies in the hundred microsecond range

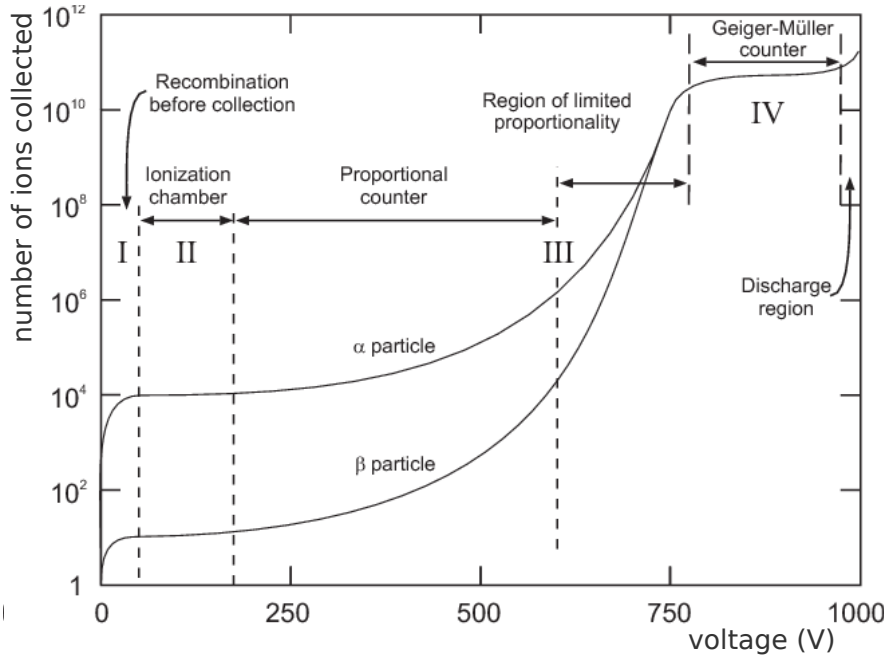

Figure IV.2.: *The diagram shows the modes of operation of a counter tube plotting the applied voltages versus the number of collected ions [Mel66].*

avalanche multiplication is the process of collision. An electron will collide after a mean free path of $1/\alpha$ producing an electron-ion pair. α is called the first Townsend coefficient. Considering an homogeneous electric field with n electrons at a certain position x, after a distance dx, one obtains an increase in the number of electrons of

$$dn = n\alpha\, dx \;\Rightarrow\; n = n_0\, e^{\alpha x}. \tag{IV.11}$$

The multiplication factor M, which is also called gas gain, is then defined as the number of created electrons divided by the number of initial electrons [Sau77].

$$M = \frac{n}{n_0} = e^{\alpha x} \tag{IV.12}$$

In case of an inhomogeneous electric field, α is dependent on x ($\alpha = \alpha(x)$) and the multiplication factor must be determined via

$$M = \frac{n}{n_0} = e^{\int \alpha(x) dx}. \tag{IV.13}$$

The avalanche process will cause a distribution similar to a drop, with electrons at the front and ions tailing behind, because ions drift about a thousand times slower than electrons. The drop will surround the wire due to lateral diffusion as shown in figure IV.3 [Leo87].

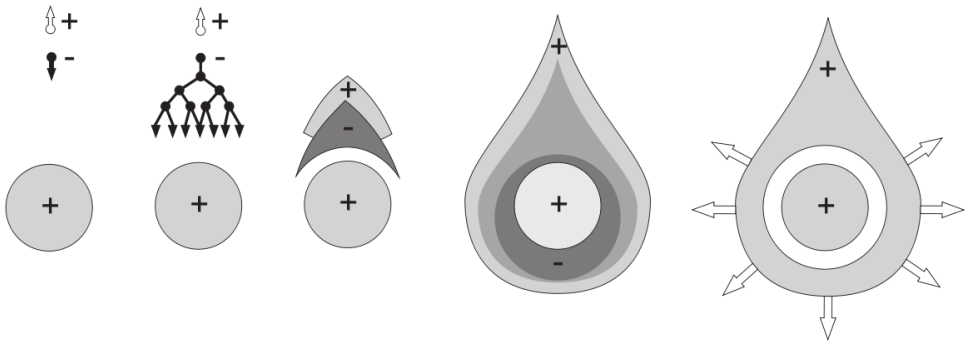

Figure IV.3.: *Development of an avalanche in a proportional counter [Cha72]. The collision of an electron produces an electron-ion pair. Close to the wire, the electron will cause an avalanche with electrons in the front and ions tailing behind. Finally, the drop will surround the wire due to lateral diffusions.*

The first Townsend coefficient is given by

$$\alpha = N\,\sigma(\varepsilon). \tag{IV.14}$$

N is the number of atoms per unit volume. For noble gases and standard states, N equals $2.69 \times 10^{19}\,\mathrm{atoms/cm^3}$. The cross section $\sigma(\varepsilon)$ can be deduced from the Ramsauer curve in figure IV.4 (left). It increases with increasing electron energy reaching a maximum around $\varepsilon = 110\,\mathrm{eV}$. Additionally, figure IV.4 (right) shows the first Townsend coefficient as a function of the reduced electric field. P corresponds to the gas pressure. For small values of α, the distribution can be approximated exponentially [Kor46].

$$\frac{\alpha}{P} = A\,e^{-BP/E} \tag{IV.15}$$

Examples for the value of the constants A and B are given in table IV.1. For higher electric fields this approximation is unsatisfying. Therefore, one assumes α to be linearly

Table IV.1.: *Values of the constants A, B, and k for several noble gases [Sau77].*

Gas	A / Torr/cm	B / Torr V/cm	k / $\mathrm{cm^2/V}$
He	3	34	0.11×10^{-17}
Ne	4	100	0.14×10^{-17}
Ar	14	180	1.81×10^{-17}
Xe	26	350	
CO_2	20	466	

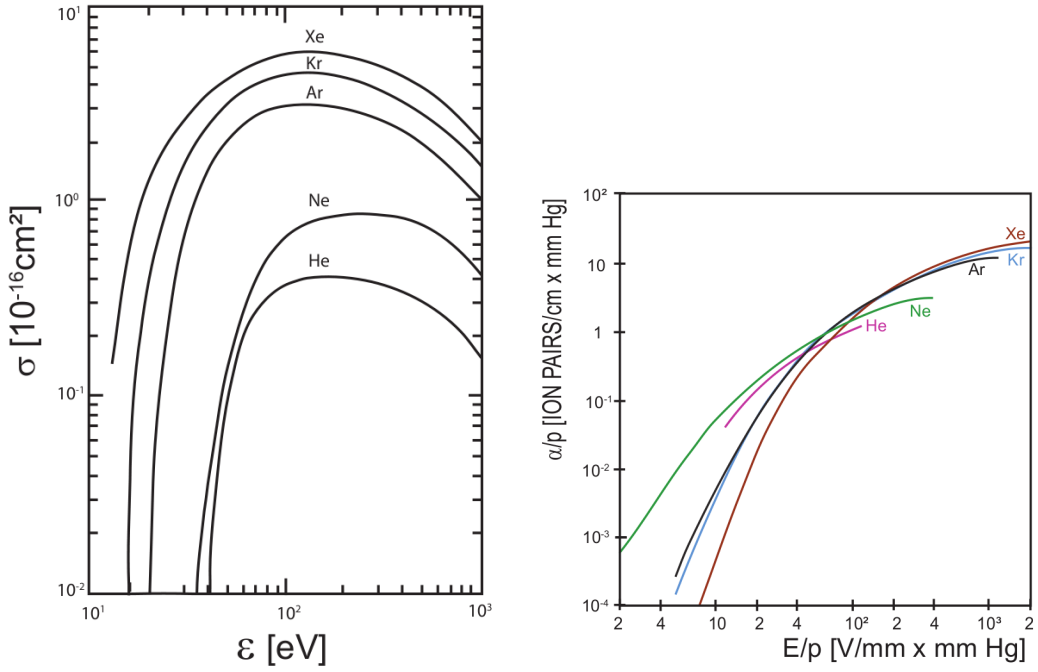

Figure IV.4.: *Left: The Ramsauer curve shows the electron energy ε plotted versus the collision cross section σ of several noble gases [All69].*
Right: First Townsend coefficient as a function of the reduced electric field for several noble gases [Bro59].

dependent on the electron energy. Furthermore, the average electron energy ε between two collisions is $^{E}/_{\alpha}$. With equation IV.3, one obtains [Sau77]:

$$\alpha = kN\varepsilon = \sqrt{kNE} = \sqrt{\frac{kNCU}{2\pi\epsilon_0\rho}} = \alpha(\rho) \; . \tag{IV.16}$$

The values for the constant k are given in table IV.1. If the Townsend coefficient is known, the multiplication factor can be calculated. Assuming the multiplication starts at a distance r from the wire, when the electric field E_c is strong enough and the threshold voltage V_T is reached, it depends exponentially on the charge per unit length $Q = CU$.

$$M = k\, e^{CU} \tag{IV.17}$$

The calculated avalanche multiplications match the measured values well, at least for moderate gains.
In case of gas mixtures, the Townsend coefficient is more difficult to fix, but generally adding polyatomic gas necessitates a larger electric field to obtain a certain value of α.

IV.4. Characteristics of gases

As avalanche multiplication occurs in noble gases at lower fields than in polyatomic gases, a noble gas is the gas of choice when building a proportional counter. Polyatomic gases need higher electric fields due to their non-ionizing energy dissipation modes.

In many proportional chambers, argon is the main component because xenon and krypton are much more expensive. Unfortunately, gains in an argon-filled chamber are limited to 10^3 - 10^4. At higher gains, a permanent discharge will occur because excited atoms of noble gases formed in the avalanche can only deexcite by emitting photons with a minimum energy of 11.6 eV. This minimum energy is high enough to extract metal electrons (Cu: 7.7 eV) from the cathode, which cause further avalanches.

A second occurrent effect is caused by the ions which are neutralized at the cathode extracting an electron. The balance of energy is either radiated or causes secondary emission at the cathode surface. This will result in new avalanches and probably in a permanent discharge.

These permanent discharges can be avoided by adding some polyatomic gas. Polyatomic gases have multiple non-radiative excited states (rotational and vibrational) being able to absorb the emitted photons. The excited molecules release the additional energy either by elastic collisions or by dissociation into smaller molecules. This way, the possible gain can reach values of 10^6. Furthermore, the neutralization at the cathode of the polyatomic gas will result in dissociation or polymerization. Consequently, the probability to induce further electrons is quite small. Polyatomic gases with these properties are called quenchers.

The quenching efficiency depends on the number of atoms in a molecule. Isobutane, containing ten atoms, is preferably used for high-gain and stable operations, whereas carbon dioxide, containing only three atoms, occasionally causes discharges. However, carbon dioxide still has a very low chemical reactivity, non-flammability, and good aging properties. Further suitable gases used in a proportional chamber are organic compounds of the hydrocarbon and alcohol family and inorganic compounds like freons, BF_3, and others. These gases display their quenching properties already when added in very small amounts.

In general, addition of electronegative gases like freons causes the highest gains because besides absorbing photons, they are also able to trap electrons extracted from the cathode before reaching the anode causing avalanches. It is important to add only small amounts of electronegative gases because they can also capture primary electrons

accordingly reducing efficiency.

Although isobutane is well suited for high-gain operations, organic gases have the disadvantage of polymerization. The built polymers attach to cathode (or anode) creating a thin layer of insulator. This causes positive ions, created by avalanches, to deposit on the layer only slowly leaking through it to be neutralized. In case of detected fluxes above 10^2 - 10^3 $^{\text{counts}}/_{\text{s cm}^2}$, the production rate will overcome the leakage rate, which results in a high density of charge on the layer. The created dipole field can reach values high enough to extract electrons from the cathode through the insulator causing permanent discharges. These discharges can only be stopped by suppression of the counter voltage. However, there is permanent damage due to this and lower fluxes will restart the discharge as long as the counter has not been completely cleaned.

Proportional counters need to operate with a continuous gas flow because a sealed counter will at some time run out of quencher and change its operational characteristics [Sau77] [Leo87].

V

Multi Wire Proportional Chamber

Due to the fact that our interest focuses on the development of a small animal PET based on multi wire proportional chambers, this chapter will explain their very basic principle of operation to understand the concept of the setup of a MWPC and the principle of the induction of a signal. Some more information is given on the specific signal induction on a wire and on the cathode pads of a MWPC. Additionally, a few words describe the various methods of the calculation of the displacement of the charge induced on a cathode pad.

V.1. Basic configuration

A MWPC consists of many parallel and equally spaced anode wires each acting as an independent counter. They are arranged in a plane centered between two cathode planes. The anode wires are held on positive potential, whereas the cathode planes are usually grounded. This results in an electric field shown in figure V.1. The field lines proceed mostly parallel converging at the anode wires.

V.2. Signal induction

V.2.1. Principle of signal induction by moving charges

The fact of moving charges to produce a signal on electrodes is demonstrated in figure V.2. An effective way of calculating the distribution of charge is presented by [Blu08] and is known as the *principle of signal induction by moving charges*.
If a point charge Q is located within a certain distance $z = z_0$ from a metal plate, it will induce a surface charge. The surface charge density σ can be calculated by using

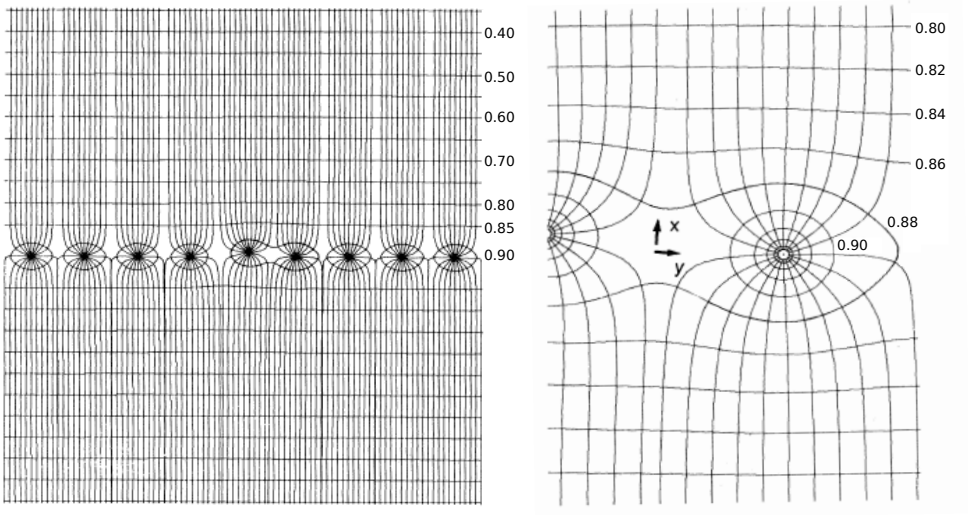

Figure V.1.: *Left: Equipotential and electric field lines of a MWPC; in the middle a shift of a wire is demonstrated having no effect on the field surrounding the wire.*
Right: Equipotential and electric field lines around a wire (spacing 2 mm, diameter 20 μm) [Cha93].

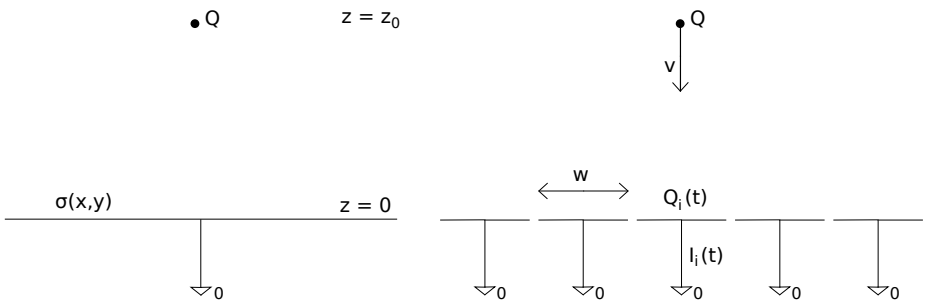

Figure V.2.: *Left: Point charge inducing a charge density on a surface of a grounded plate.*
Right: Subdivision of the plate into strips; Movement of the point charge causes changing induced charges and hence a current flowing between strip and ground [Blu08].

the method of images with a mirror charge $-Q$ at $z = -z_0$ and is given by:

$$\sigma_z(x,y) = \frac{Qz_0}{2\pi\left(x^2+y^2+z_0^2\right)^{3/2}}\,, \qquad \sigma_x = \sigma_y = 0\,. \tag{V.1}$$

The total charge induced on the surface Q_{surface} is obtained by integrating equation V.1. It is independent of the distance of the point charge.

$$Q_{\text{surface}} = \int_{-\infty}^{\infty}\int_{-\infty}^{\infty} \boldsymbol{\sigma}(x,y)\,dxdy = -Q \tag{V.2}$$

By subdividing the cathode plane into strips of width w, the induced charge on the i-th cathode strip Q_i is dependent on the distance z_0 and it is given by:

$$Q_i(z_0) = \int_{-\infty}^{\infty}\int_{-w/2}^{w/2} \boldsymbol{\sigma}(x,y)\,dxdy = \frac{-2Q}{\pi}\,\arctan\left(\frac{w}{2z_0}\right). \tag{V.3}$$

If the charge moves with the velocity v, z_0 will become time-dependent $z_0(t) = z_0 - vt$. The induced charge Q_i is then time-dependent inducing a current $I_i(t)$.

$$I_i(t) = -\frac{d}{dt}Q_i[z_0(t)] = -\frac{\partial Q_i[z_0(t)]}{\partial z_0}\,\frac{\partial z_0(t)}{\partial t} = \frac{4Qw}{\pi\left(4z_0^2(t)+w^2\right)}\,v \tag{V.4}$$

The principle of signal induction by moving charges gives an expression for the induced current using a simple geometry. In the case of signal induction of a MWPC, the calculation becomes more complex.

V.2.2. Signal induction on a wire of a MWPC

Assuming that all wires N are held on the potential U_n, the charges q_n on the wires can be calculated with the capacitance matrix given in equation V.5 [Blu08].

$$q_n = \sum_{m=1}^{N} c_{nm}U_m \tag{V.5}$$

For the following calculation, the cathode plane is considered to be electrode one, whereas the wires are indicated as electrode two, three, etc. being infinitely long. As long as the radius ρ is much smaller than the distance between the chamber electrodes, the calculation for the electric field made in section IV.1 is still valid. The electric field is then given by

$$E(\rho) = \frac{q_n}{2\pi\epsilon_0\rho} = \frac{1}{2\pi\epsilon_0\rho}\left(\sum_{m=1}^{N} c_{nm}U_m\right) \tag{V.6}$$

Furthermore, equation IV.8 and IV.9 are transferable. If the ion trajectory is known, the weighting fields of the wires are used to find an expression for the induced current. This weighting field of an electrode is determined by applying a voltage V_w to the electrode of interest and grounding all others. The induced current of all wires is finally given by:

$$I_w(t) = \sum_{n=2}^{N} I_n(t) = -\frac{N_{\text{tot}} e_0}{4\pi\epsilon_0} \frac{1}{t+\bar{t}_0} \sum_{n=2}^{N} c_{1n} = -\frac{N_{\text{tot}} e_0}{4\pi\epsilon_0} \frac{C_{12}}{t+\bar{t}_0} \,. \tag{V.7}$$

N_{tot} is the total number of ions with charge $+e_0$ building the avalanche and $\bar{t}_0$ is defined as:

$$\bar{t}_0 = \frac{R_1^2}{\mu U} \frac{\pi\epsilon_0}{C_{12}} \,. \tag{V.8}$$

It is remarkable that this result is similar to the current induced in a counter tube I_{ct} [Blu08].

$$I_{\text{ct}} = -\frac{N_{\text{tot}} e_0}{2\ln(R_2/R_1)} \frac{1}{t+t_0} \tag{V.9}$$

V.2.3. Signal induction on a cathode pad of a MWPC

Since the wire plane is enclosed by the cathode planes and the law of charge retention holds, the signal on a single cathode $I_{c_i}(t)$ equals half of the negative sum of the signal on the wires $I_w(t)$.

$$I_{c_1}(t) = \frac{1}{2} I_c(t) = -\frac{1}{2} I_w(t) = \frac{1}{2} \frac{N_{\text{tot}} e_0}{4\pi\epsilon_0} \frac{C_{12}}{t+\bar{t}_0} \tag{V.10}$$

A method to calculate the signal on a cathode strip of width w is demonstrated by *Mathieson* and *Gordon* [Mat84]. It makes use of the weighting field of the strips and suggests some approximations like neglecting the influence of an avalanche which would develop unsymmetrically around the wire.

The idea is to calculate the signal on a cathode strip of infinitesimal width first, followed by an integration over the full width w. The first step to solve the problem is to define the cathode charge distribution $\Gamma(\lambda)$ with $\lambda = x/h$, the distance of the infinitesimal strip from the avalanche position.

$$dI_{c_1}(t,\lambda) = I_c(t)\,\Gamma(\lambda)\,d\lambda \qquad \int_{-\infty}^{\infty} \Gamma(\lambda)\,d\lambda = \frac{1}{2} \tag{V.11}$$

Gatti et al [Gat79] introduced a three-parameter semi-empirical expression for the cathode charge distribution.

$$\Gamma(\lambda) = K_1 \frac{1-\tanh^2(K_2\lambda)}{1+K_3\tanh^2(K_2\lambda)} \tag{V.12}$$

Equation V.11 implies that there are only two independent parameters. It is K_1 and K_2 defined by K_3.

$$K_1 = \frac{K_2\sqrt{K_3}}{4\arctan\sqrt{K_3}} \qquad K_2 = \frac{\pi}{2}\left(1 - \frac{\sqrt{K_3}}{2}\right) \tag{V.13}$$

The parameter K_3 is dependent on the MWPC geometry. In figure V.3, K_3 is shown for several MWPC geometries defined by its wire pitch s, its wire radius r_a, and the anode cathode distance h. For values of h/s smaller than 1.0, pads parallel and perpendicular to the anode wires need to be handled differently. However, for normally accessible values of $^{h}/_{s}$ and $^{r_a}/_{s}$, the values for K_3 are not very different.

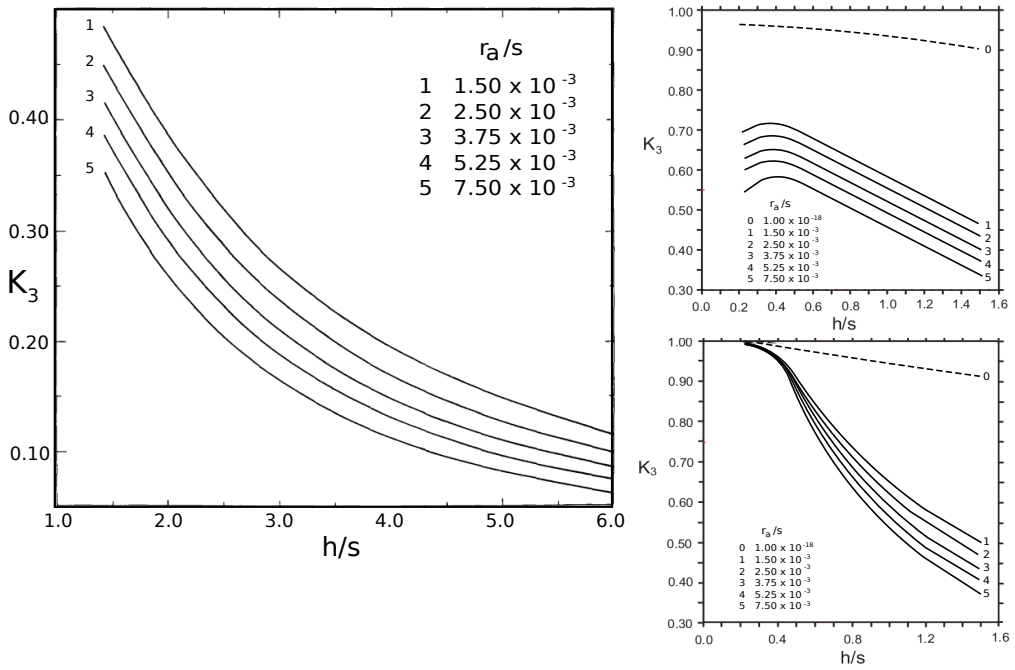

Figure V.3.: *Left: K_3 for $^{h}/_{s}$ between 1.0 and 6.0.*
Right: K_3 for cathode pads parallel to the anode wire direction (top) and K_3 for cathode pads normal to the anode wire direction (bottom) for $^{h}/_{s}$ between 0.0 and 1.6 [Mat88].

The current induced on a cathode strip of width w centered at position λ is determined by solving the integral of equation V.11. The result of the integral of the cathode charge distribution over the pad width w is known as the *pad response function* (PRF) $P_0(\lambda)$. The induced current $I(t,\lambda,w)$ is finally given by [Blu08]

$$I(t,\lambda,w) = I_c(t) \int_{\lambda-w/2}^{\lambda+w/2} \Gamma(\lambda')\, d\lambda' = I_c(t)\, P_0(\lambda) \tag{V.14}$$

with the pad response function

$$P_0(\lambda) = \frac{K_1}{K_2\sqrt{K_3}}\Bigg(\arctan\left[\sqrt{K_3}\tanh\left(K_2(\lambda+\frac{w}{2})\right)\right] - \arctan\left[\sqrt{K_3}\tanh\left(K_2(\lambda-\frac{w}{2})\right)\right]\Bigg). \tag{V.15}$$

V.3. Calculation of the displacement

The displacement x is defined as the distance from the center of a pad to the arrival position of the avalanche detecting the charge Q_i. To calculate the displacement of the induced charge on the cathode strip, there are several methods which were discussed by [End81]:

a) *unweighted* displacement function

b) *weighted* displacement function

c) *center of gravity* of the charges of three pads

d) *center of gravity* of the charges of five pads

e) *Lorentzian* curve fitting

f) *Parabolic* curve fitting

For the derivation of the unweighted (a) and weighted (b) displacement function, a Gaussian fit can be used to approximate the PRF. It is

$$P_0(x) \sim e^{\frac{-x^2}{2\sigma^2}}. \tag{V.16}$$

There is also a direct proportionality between the PRF and the charge induced on a pad. In the case of the displacement function, three adjacent pads are considered with Q_i marking the pad of maximal charge.

$$\begin{aligned} Q_{i-1} &\sim e^{\frac{-(x+w)^2}{2\sigma^2}} \\ Q_i &\sim e^{\frac{-x^2}{2\sigma^2}} \\ Q_{i+1} &\sim e^{\frac{-(x-w)^2}{2\sigma^2}} \end{aligned} \tag{V.17}$$

To find the displacement x of a signal independent of σ, the following ratios of charges are looked upon and solved for x.

$$\frac{Q_{i+1}}{Q_{i-1}} = e^{\frac{2xw}{\sigma^2}} \qquad \frac{Q_i^2}{Q_{i-1}Q_{i+1}} = e^{\frac{w^2}{\sigma^2}} \tag{V.18}$$

$$\Longrightarrow x_{\text{unweighted}} = \frac{w}{2}\frac{\ln\left(Q_{i+1}/Q_{i-1}\right)}{\ln\left(Q_i^2/Q_{i-1}Q_{i+1}\right)} \tag{V.19}$$

This equation is called the *unweighted displacement function*. Based on the unweighted displacement function, the weighted displacement function can be calculated by determining σ and regarding the ratios of charges of two adjacent pads:

$$\frac{Q_i}{Q_{i-1}} = e^{\frac{2xw+w^2}{\sigma^2}}, \qquad \frac{Q_{i+1}}{Q_i} = e^{\frac{2xw-w^2}{\sigma^2}}. \tag{V.20}$$

Solving for x gives:

$$x = \frac{\sigma^2}{w}\ln\left(\frac{Q_i}{Q_{i-1}}\right) - \frac{w}{2}, \qquad x = \frac{\sigma^2}{w}\ln\left(\frac{Q_{i+1}}{Q_i}\right) + \frac{w}{2}. \tag{V.21}$$

The advantage of this approach is that each equation depends only on the charge of two adjacent pads. Intending to improve spatial resolution, a combination of these two equations for x is used weighting each term with a weighting factor (w_1 and w_2). In most cases, these weighting factors are defined as:

$$\omega_1 = Q_{i-1}^2, \qquad \omega_2 = Q_{i+1}^2.$$

Assuming, there will be a signal on only two pads, equation V.19 becomes inaccurate, but can determine an appropriate σ to solve the *weighted displacement function*:

$$x_{\text{weighted}} = \frac{1}{\omega_1+\omega_2}\left[\omega_1\left(\frac{\sigma^2}{w}\ln\left(\frac{Q_i}{Q_{i-1}}\right) - \frac{w}{2}\right) + \omega_2\left(\frac{\sigma^2}{w}\ln\left(\frac{Q_{i+1}}{Q_i}\right) + \frac{w}{2}\right)\right]. \tag{V.22}$$

In this case, if only two pads are significantly activated, the weighting will shift the calculation towards the right side. However, the appropriate determination of σ is mandatory for any improvement in resolution.
The unweighted and weighted displacement function are the most common methods of determining the displacement of a signal on the cathode pad, but there are alternatives. Determining the displacement using the center of gravity method (c) and (d), the centroid can be calculated using more than three pads. Here, either three (eq. V.23) or five (eq. V.24) adjacent pads are considered.

$$x_3 = w\,\frac{-Q_{i-1}+Q_{i+1}}{Q_{i-1}+Q_i+Q_{i+1}} \tag{V.23}$$

$$x_5 = w\,\frac{-2Q_{i-2}-Q_{i-1}+Q_{i+1}+2Q_{i+2}}{Q_{i-2}+Q_{i-1}+Q_i+Q_{i+1}+Q_{i+2}} \tag{V.24}$$

In addition to the Gaussian curve fitting, one can also make use of the Lorentzian (e) and parabolic (f) curve fitting methods. Again, there are three points to calculate a suitable fit. The functions are given by

$$x_{\text{lorentzian}} = w \, \frac{\frac{1}{Q_{i-1}} - \frac{1}{Q_{i+1}}}{2(\frac{1}{Q_{i-1}} - \frac{2}{Q_i} + \frac{1}{Q_{i+1}})} \tag{V.25}$$

$$\text{and} \quad x_{\text{parabolic}} = w \, \frac{Q_{i-1} - Q_{i+1}}{2(Q_{i-1} - 2Q_i + Q_{i+1})} \, . \tag{V.26}$$

VI

Geant4 Simulations

Since the lack of support and service of the quadHIDAC will make its future operation in Muenster difficult, a project to develop a high-resolution Small Animal PET based on MWPC, hosted by the Sonderforschungsbereich 656 "Molecular Cardiovascular Imaging", has been launched. Part of it focuses on the development of a new technique to optimize and manufacture photon-to-electron converters because these are essential for the detection process.
Before the manufacturing process of a new photon-to-electron converter can be started, there are many decisions which have to be made. There is definitely the technical feasibility indicating limits, but it is also necessary to evaluate considering simulations. Simulations will help to get an understanding of the design and its main factors which must be considered when finding compromises for the final manufacturing design. This chapter will deal with converter related simulations using Geant4 and give an idea of the importance of certain converter parameters.

VI.1. The program

The program *Geant4* is consists of plenty of software packages, which all together are able to simulate the transition of particles through matter. Due to the large amount of simulation parameters, the software is divided into small logical units. This simplifies the application for the user because different parts of the simulation setup can be handled independently without interference. By setting `C++`-based class categories, the logical units are built. Class categories have some relationship within the limits of keeping track. Figure VI.1 shows the different class categories of Geant4 and its relation marked by straight lines. The circles indicate that this very class category uses the

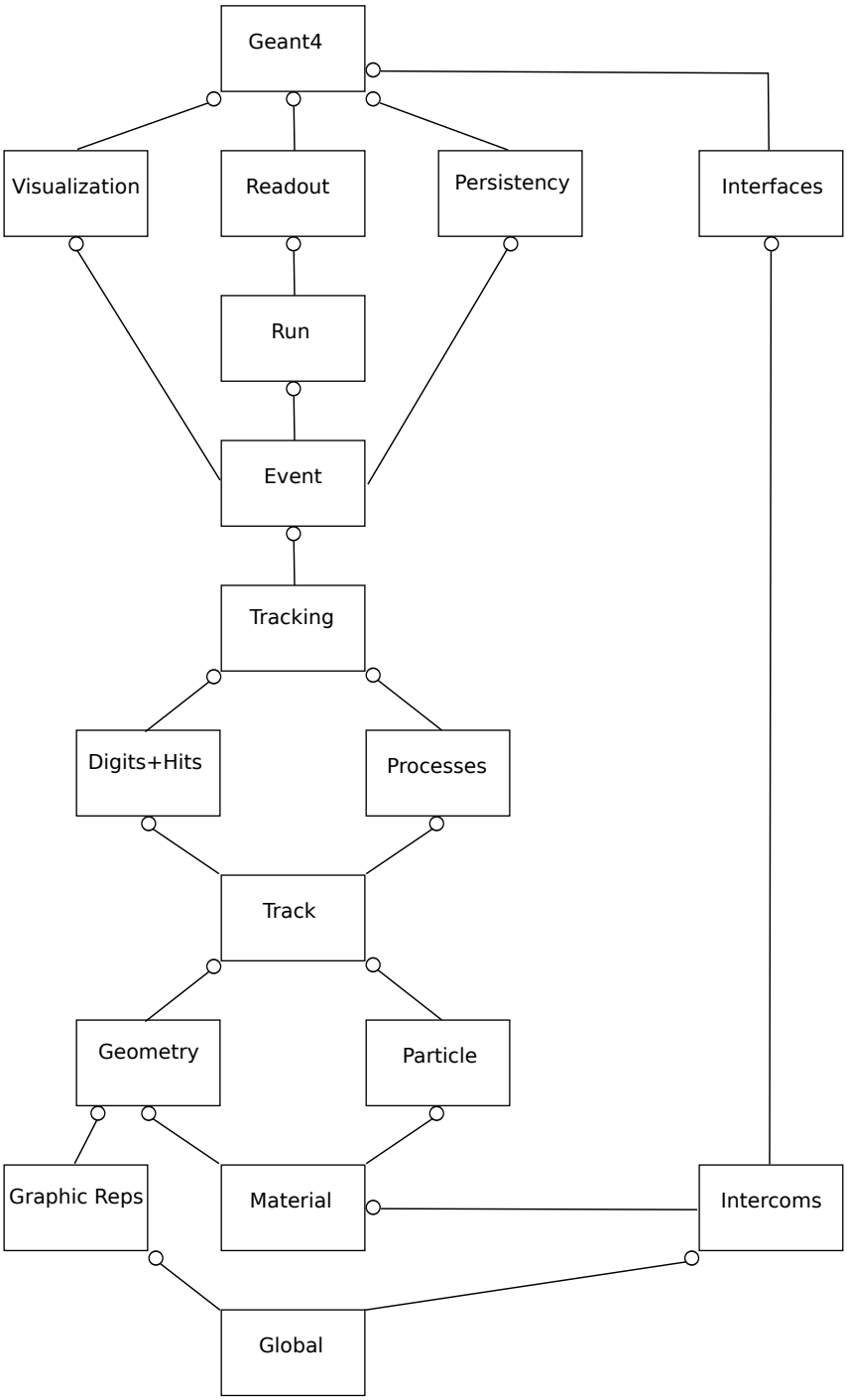

Figure VI.1.: *Geant4 is a software system divided into small logical units. The relations between the class categories are marked by straight lines. The circles indicate that this class category makes use of the class category at the end of the line.*

class category at the end of the line.
Basically, there are two different types of classes. There are those which are needed before a run is started, called initialization classes, and those which define the run itself, called action classes. The initialization is executed by the command */run/initialize*. At this point, geometry, materials, particles, and physics are set and the program switches into *Idle*. In this state, runs can be started using */run/beamOn [number]*, which calls the action classes.

VI.1.1. Class categories

Initialization

- *Detector Construction*
  The detector construction class handles definitions of materials, geometries and visualization. The geometry is set by defining volumes. Geant4 provides the most common volumes like spheres, cylinders, boxes, and so on. The defined volumes are placed into each other, and one speaks of placing *daughter-* into *mother volumes*. The main volume is called the *world volume* limiting the dimensions of the simulation. Every volume declaration is divided into three steps. Step one is the setting of the basic geometry called solid volume. Step two is the definition of the material of the solid volume, which makes a logical volume. In step three, the logical volume can be placed into a mother volume, and a physical volume is created. Logical volumes can be placed several times, but overlaps must be taken care of. In the end, the visualization for every logical volume can be asked for explicitly. Optionally, an electric or magnetic field can be initialized.

- *Physics List*
  The physics list class handles all physical processes which are necessary for the simulation. Additionally, every particle generated in the simulation needs to be defined. For these implementations, Geant4 provides most of the common physical processes and definitions of elementary particles. It is further possible to abort physics processes or particle transport and set energetic thresholds called production cuts.

Action

- *Primary Generator Action*
  The primary generator class sets the primary beam particles, their energy, and

their direction.

- *Run Action*
  The run action class can be compared to a real experimental run. It is the largest unit of the simulation. A run consists of a set of events with stable framework conditions regarding geometry and physics. The main class calls the run action class to control the simulation by returning the detector construction and guiding the event action.

- *Event Action*
  The event action buffers all primary particles in a stack at the beginning of an event. In a last-in-first-out-manner, event per event is sent to the tracking manager for further analysis. The event manager cares about secondary particles, which are tracked in the same way.

- *Stacking Action*
  The stacking action class pops tracks from the stack until it is empty and a new event can be generated.

- *Tracking Action*
  The tracking action class handles the information of a particle traveling in space and time. It deletes a track as soon as the particle decays, has lost its kinetic energy or leaves the world volume. Therefore, it is necessary to store the relevant information in trajectory objects for later analysis. A track is calculated by using the stepping action class.

- *Stepping Action*
  The stepping action class defines the step which is the unit of particle movement. With the knowledge of the *PreStepPoint*, it can calculate the *PostStepPoint* by considering energy, direction, and cross section.

VI.2. Design of the quadHIDAC

The quadHIDAC (HIgh Density Avalanche Chamber) consists of 32 modules arranged in a circular geometry of four detector blocks, each holding eight modules (see figure VI.2). This gantry makes up a cylindrical field of view (FOV) with a length of 280 mm and a diameter of 165 mm.

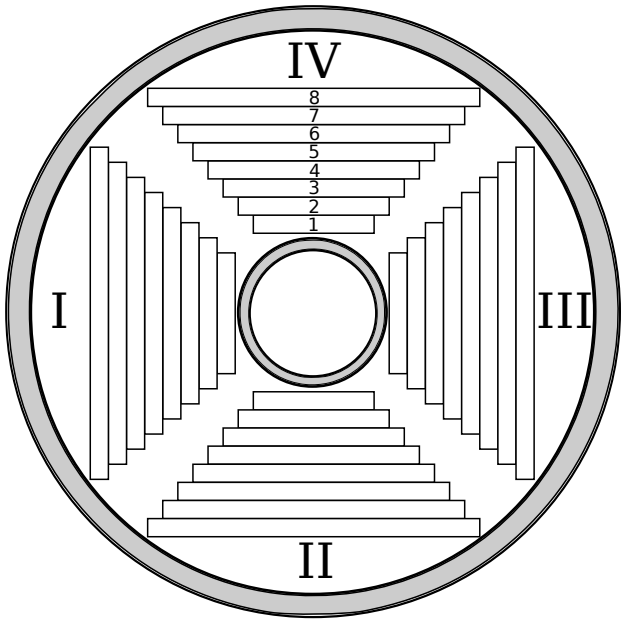

Figure VI.2.: *The gantry geometry of the 32-module quadHIDAC Small Animal PET scanner. It consists of four detector banks holding eight modules each.*

The modules have dimensions varying from $(135 \times 280)\,\mathrm{mm}^2$, for the one closest to the center, to $(271 \times 280)\,\mathrm{mm}^2$, for the furthest module, to prevent loss of sensitivity due to undetectable photon trajectories. Here, the sensitivity is defined as the ratio of detected decays to the overall number of decays in the FOV.

Each module of the quadHIDAC consists of a MWPC represented by a layer of anode wires sandwiched between two cathode pad planes. On the outside of the cathode planes, a photon-electron converter is installed as shown in figure VI.3 (left). This converter is made of a stack of 16 layers of lead of 60 µm, each staggered with 140 µm-layers of insulator material. The converter has been mechanically drilled holding 400 µm holes at a 500 µm pitch. The top layer of each converter is a plane 50 µm-layer of lead covered with a 200 µm layer of plastics, which isolates and seals. The layers of lead are held on cascading potentials applied by a resistor chain on the outside of the modules. This way the top layer receives a potential of -3000 V, which drops down to -200 V for the bottom layer. The electrons which are knocked out of the lead by the photons are drifted through the holes towards the anode wires. The electric potential of the anode wires of 2000 V focuses the electrons, which start avalanching very close to the wire (see section IV.3).

The quadHIDAC modules are filled with a gas mixture of argon, quenching gas and diisopropylether.

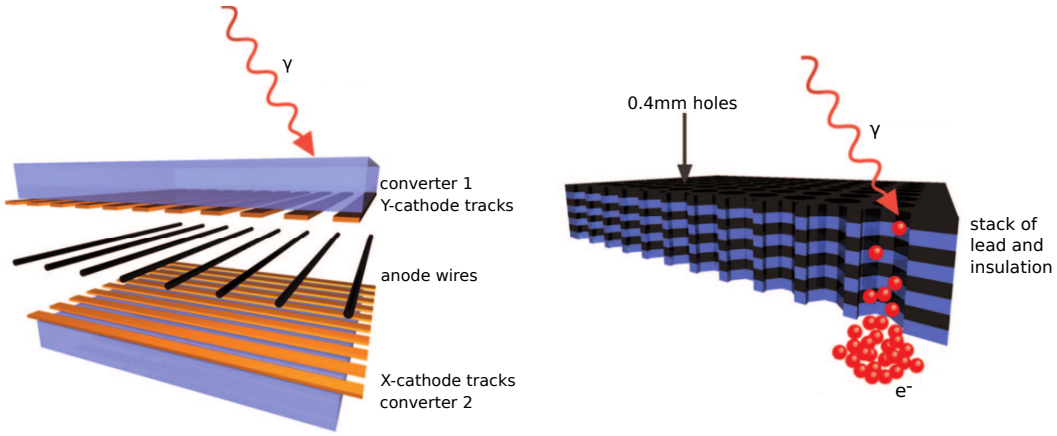

Figure VI.3.: *Left: The rough design of a single module of the quadHIDAC: the MWPC in between two converters.*
Right: The converter consists of a stack of interleaved lead and insulation layers which convert the incoming photon into an electron. The densely drilled matrix design of the holes in combination with the applied cascading potential on the lead layers will lead the electron into the MWPC. If the electric field strength is high enough, the electron will cause avalanche multiplication [Sch05].

VI.3. Simulation of the quadHIDAC

The original simulation code of the quadHIDAC Small Animal PET scanner was set up by *Holger Gottschlag* [Got10]. The simulation design is based on the descriptions of [J+99],[Jea95],[Jea02], and [Sch05]. While Gottschlag performed simulations to get a better understanding of the scanner's behavior, the focus of this work will be on the evaluation of converter setups.

VI.3.1. The new simulation code

The simulation code implemented by Gottschlag has been well developed giving reliable results. However, there are disagreements regarding the original geometry of the quadHIDAC [Got10]. In order to obtain better results, the code has been modified to a more realistic configuration.
In the modified code, an extension has been implemented regarding the detector blocks. It is currently possible to simulate all four detector blocks at a time [Ver11]. Before, the simulation had been restricted to only use two blocks. As the implementation of the code has additionally been optimized, the simulation of four detector blocks is now

running comparatively fast and stable.
The first module of each detector block is placed at a distance of 89.8 mm from the center, which results in an overall FOV of $322.27\,\mathrm{cm}^2 \times 280.00\,\mathrm{mm}$ depth.
Since Geant4 is not capable of handling avalanche propagation of electrons in electric fields, the detector response is not original. The present code selects and saves a hit if an electron crosses the geometrical border between any volume and the gaseous volume of the modules. Gaseous volumes are implemented for the holes and the wire chamber. The entire event consisting of event number, block (I - IV) and module number (1 - 8) of the event (see figure VI.2), kinetic energy and vertex point of the electron plus information about the mother particle is saved in a ROOT tree.
In the following, each simulated data point was determined with a statistic of 5,000,000 events. Therefore, the statistical error becomes small varying between minimal 0.05 % and maximal 0.12 %.

VI.3.2. Converter configuration

As the converter draws particular interest, it was also necessary to make significant changes on the implemented converter geometry of the existing simulation. This new converter configuration consists of holes arranged in a three-cornered configuration. It is seen in figure VI.4 (right), next to the old geometry. Figure VI.5 shows a $(5 \times 5)\,\mathrm{mm}^2$ cut of the entire converter as it is programmed at present.

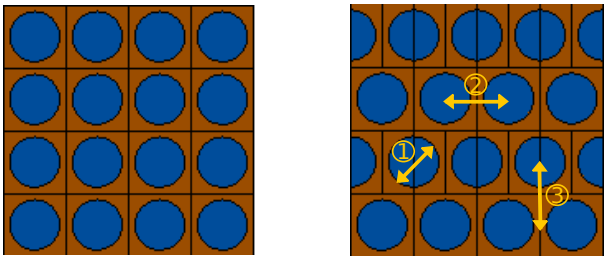

Figure VI.4.: *Left: The parallel arrangement of the holes in the converter as it has been implemented by Gottschlag. The crossings of the black lines indicate simulation based concentrations of lead.*
Right: The current displaced arrangement of the holes in the converter with the numbers indicating: ① diameter of holes, ② distance of holes in one direction, ③ distance of holes in second direction.

It is indicated in figure VI.4 that there are many parameters regarding the converter which can affect the sensitivity. There is the hole diameter ①, the hole distance in

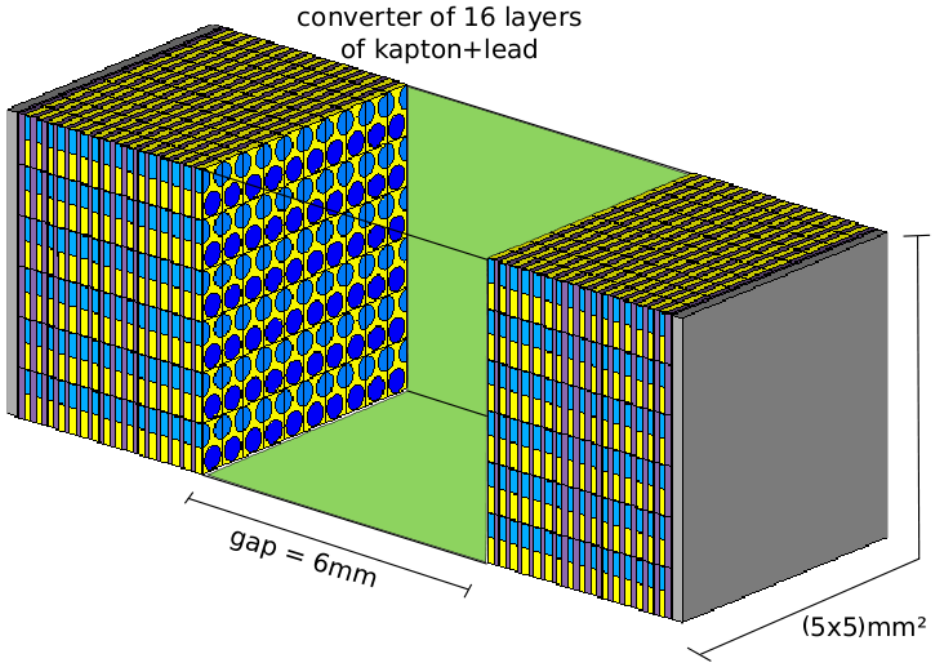

Figure VI.5.: *The converter consists of 16 layers of alternating lead (violet) and kapton (yellow) penetrated with holes (blue). The outsides of the converter are covered with a 200 µm foil of plastic (gray) and a plane lead layer of 50 µm. The gap (green) between the two converter parts building a module is 6 mm and filled with a gas mixture.*

x-direction ②, and the hole distance in y-direction ③. Besides, the effects of varying the converter thickness can be looked at, which means in particular changing the thickness of insulation and lead layers. These layers are implemented as kapton and lead foils.
In this context, there are two effects which will affect the sensitivity: absorption of photons and emission of electrons.
The simulation of the original converter setup, with distances of holes in both directions of 500 µm, a diameter of the holes of 400 µm, and thickness of the kapton foil of 140 µm, gives a sensitivity of 6.71 %. This has to be improved.

The first attempt is to compare the parallel and the newly implemented displaced arrangement. Therefore, the converter parameters were set to original quadHIDAC sizes, except for the hole pitch. The hole pitch has been varied in this simulation because there is a special interest in the influence of the $^{\text{hole}}/_{\text{material}}$-ratio on the sensitivity. The

results of these simulations are visualized in figure VI.6.
In general, the sensitivity for the displaced arrangement is higher than the sensitivity of the parallel arrangement. This is due to the fact that if the holes are displaced, the concentration of lead material (see figure VI.4) will disappear, and less electrons will be re-absorbed in the lead of the converters.

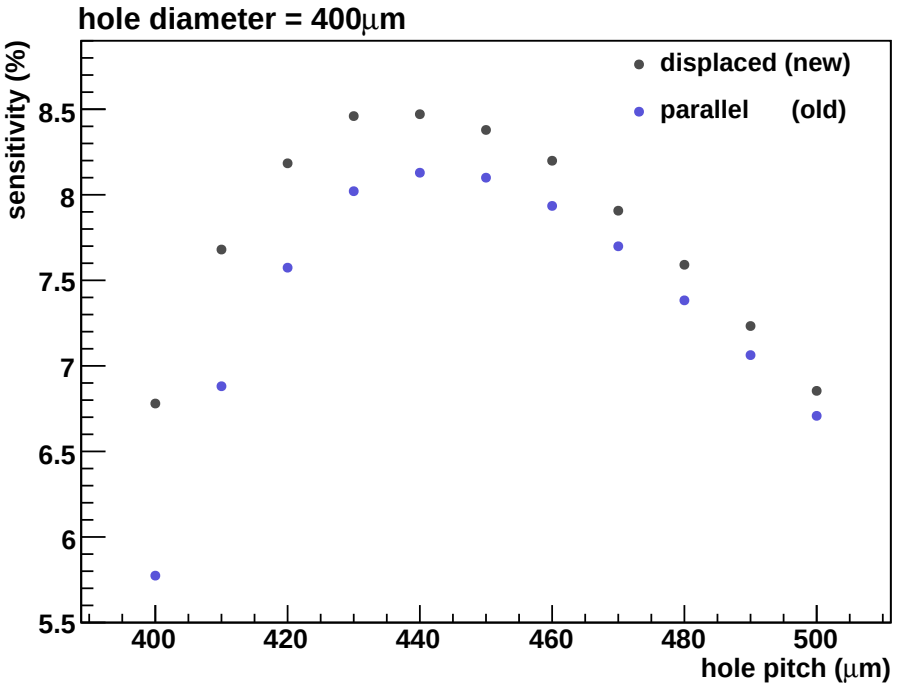

Figure VI.6.: *The sensitivity is plotted versus the hole distance for the parallel (blue markers) and the displaced (gray markers) arrangement. The sensitivity of the displaced arrangement is generally higher reaching maximal values in the interval [430 µm,460 µm].*

Furthermore, the plots in figure VI.6 show interesting results evaluating the $^{\text{hole}}/_{\text{material}}$-ratio. If this ratio increases, which comes along with a decrease of the hole distances, the sensitivity will increase, reach a maximum at some point, and decrease again. The maximum lies in the interval [430 µm,460 µm]. Considering the difficulties in manufacturing these geometries, the optimal converter configuration is set to have a hole pitch of approximately 450 µm in the case of a 400 µm hole diameter, which means there is a hole bridge of 50 µm material.

VI.3.3. Variations of thickness of the kapton foil

Motivated by the results of several simulations, it was decided to analyze the influence of the thickness of the kapton foil in more detail. The interval of interest for the thickness of the kapton foil has been set from 100 µm to 500 µm. In addition, the simulations have been run for five different hole diameters of 100 µm, 200 µm, 300 µm, 400 µm, and 500 µm. Inspired by the last section, the arrangement of the holes was displaced holding a bridge of 50 µm. A visualization of the arrangement of the holes can be seen in figure VI.7. The results of these simulations are shown in the diagram of figure VI.8.

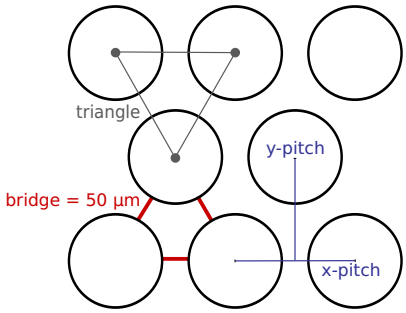

Figure VI.7.: *Visualization of the triangular arrangement of the holes indicating the parameters x-pitch, y-pitch and bridge.*

In general, the sensitivity increases with increasing kapton foil thickness reaching a plateau at approximately 300 µm. This can be explained by considering the photon-to-electron conversion. The electrons generated in the lead layer enter the kapton layer. Reaching the following lead layer, they are most likely to be re-absorbed by the lead. A thicker kapton foil will lead more electrons into the holes where they will drift towards the wires. At some point, the kapton foil reaches a size which enables all converted electron to reach the holes, and a further increase of the thickness of the kapton foil does not show any significant effect, but the sensitivity saturates.
Altogether the obtained sensitivity values in figure VI.8 show promise. Especially for small holes, the sensitivity can reach values above 10 %. Although a geometry consisting of just 100 µm holes seems very promising regarding this simulation, the real behavior of such a converter stays questionable. Due to the small dimensions of these holes, the process of gas multiplication might be affected. Whereas in 500 µm holes one electron will undergo in average one interaction producing four secondary electrons [PPB10], this interaction will seriously be suppressed in a 100 µm hole due to the size. Also it is not clear whether the secondary electrons will be able to leave the hole without being absorbed either by the gas itself or by the solids.

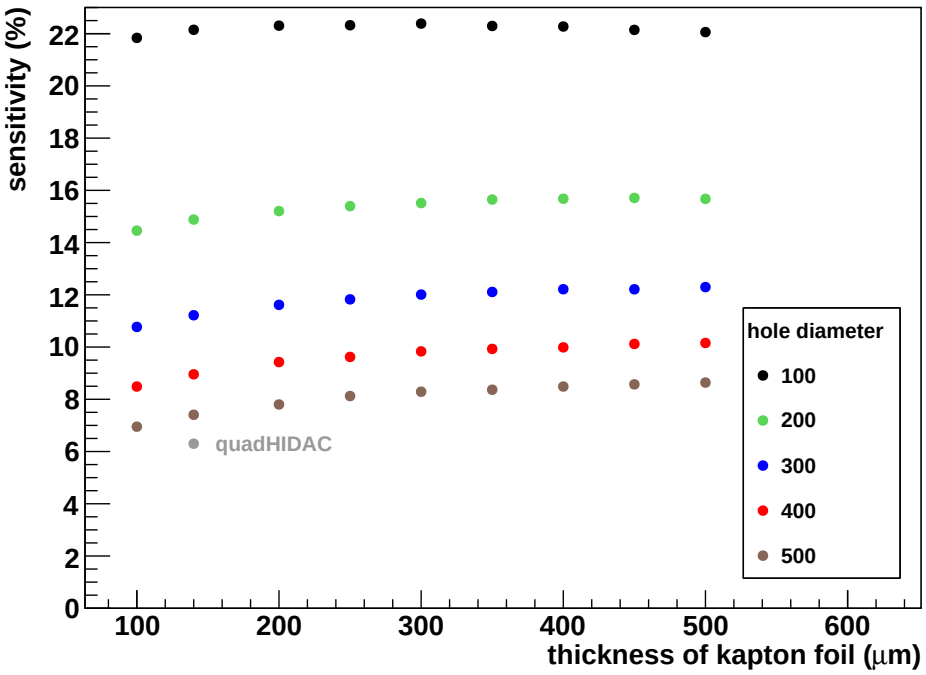

Figure VI.8.: *The obtained sensitivity is plotted versus the thickness of the kapton foil for diameters of holes varying from 100 µm to 500 µm. The arrangement of the holes is displaced with a bridge of 50 µm between two holes.*

VI.3.4. Influence of cone-shaped holes

There is a third aspect which has been taken into account. When building new converters, one might make use of laser or etching techniques. So far, the laser technique has been neglected because every attempt to create holes resulted in undefined non-circular hole setups including melting of the involved materials. Fortunately, the etching technique seems more promising at this point. Unfortunately, etching will result in cone-shaped holes in comparison to the tube-like shape resulting from drilling techniques. The current idea of the manufacturing process intends to build single combined lead-kapton layers first followed by an assembling procedure.

The cone-shaped holes have been incorporated into the simulation. The production method mentioned before allows two ways of assembly, which are shown in figure VI.9. Setup 1 consists of an opening lead hole pointing towards the wire plane, whereas setup 2 has a closing lead hole pointing towards the wires. The simulation has been run using the original quadHIDAC parameters and using the optimal hole pitch parameter. Its

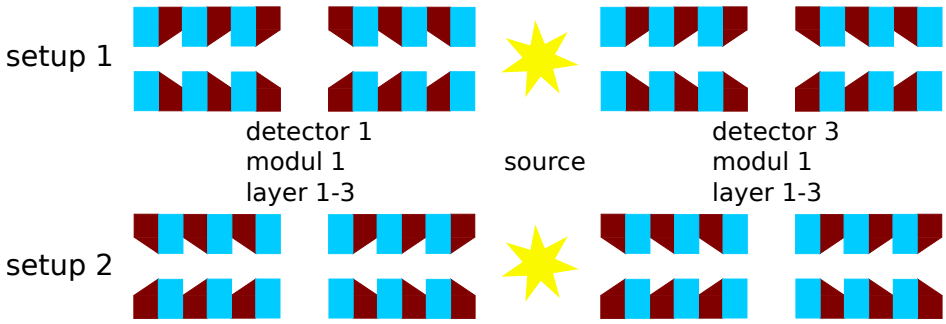

Figure VI.9.: *The planned manufacturing process proposes two different setups of assembly of the single combined lead-kapton layers. In this figure, two opposite holes are shown for the inner three layers of the two converters of a module. Lead is indicated in brown, kapton in blue.*
Top: In setup 1, the biggest lead hole radius is pointing towards the wire plane.
Bottom: In setup 2, the smallest lead hole radius is pointing towards the wire plane.

results are shown in figure VI.10.
In fact, there is even a third and fourth possible setup which would be a combination of setup 1 and setup 2. It would be possible to assemble all opening lead holes either pointing towards the source or away from the source. However, these assemblies represent averages of the results for setup 1 and setup 2 and are therefore not discussed in the following.
The results in figure VI.10 show slightly higher sensitivities for setup 2 (triangles) in comparison to setup 1 (circles). The deviation slightly increases with decreasing minimal diameter of the cone-shaped lead holes. It probably occurs because the passage from the lead volume to the gas volume is slightly more convenient, increasing, when the hole itself opens up towards the wire plane. In any case, the orientation of the cone-shape should not significantly affect the sensitivity of a module.
Generally, it turns out that the sensitivity decreases with the development of the cone-shape. This is an important fact, which must be considered when deciding on how to build a new converter.
When looking at a hole pitch of 450 µm, the effect of decreasing sensitivity almost disappears. Again, this should be taken into account when evaluating the design and manufacturing process of a new converter as a smaller hole pitch is desirable.

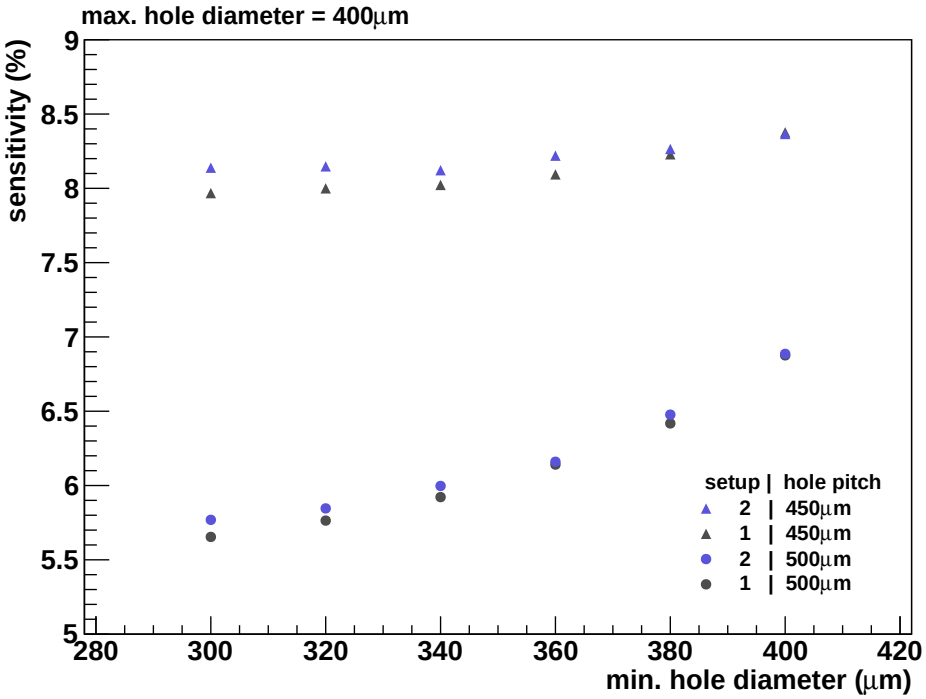

Figure VI.10.: *Geant4 simulation of the cone-shaped holes. The maximum hole diameter is held constant at 400 µm with the minimum hole diameter varying between 300 µm and 400 µm. Setup 1 and setup 2 are compared for a hole pitch of 500 µm respectively 450 µm. In general, the sensitivity decreases with the development of the cone-shape, more pronounced for a hole pitch of 500 µm than for a pitch of 450 µm.*

To complete the discussion of the influence of cone-shaped holes on the behavior of the converter, the hole geometry was implemented into *Garfield*[1]. In figure VI.11, the drift lines inside a single hole are visualized for setup 1 and setup 2 respectively.
The results of the Garfield simulation do not show differences between the drift lines for setup 1 and setup 2. This leads to the same conclusion as before: the orientation of the assembled single converter layers should not affect sensitivity.

As a reference to the electron drift lines obtained in figure VI.11, figure VI.12 shows the resulting drift lines of a simulation of a tube-shaped hole. The run inside the hole is very similar. There are few deviations for the boundary tracks, but the majority of drift lines will reach the wire plane. However, this simulation points out that electrons

[1] software for the detailed simulation of two- and three-dimensional drift chambers developed at CERN
`http://garfield.web.cern.ch/garfield/`

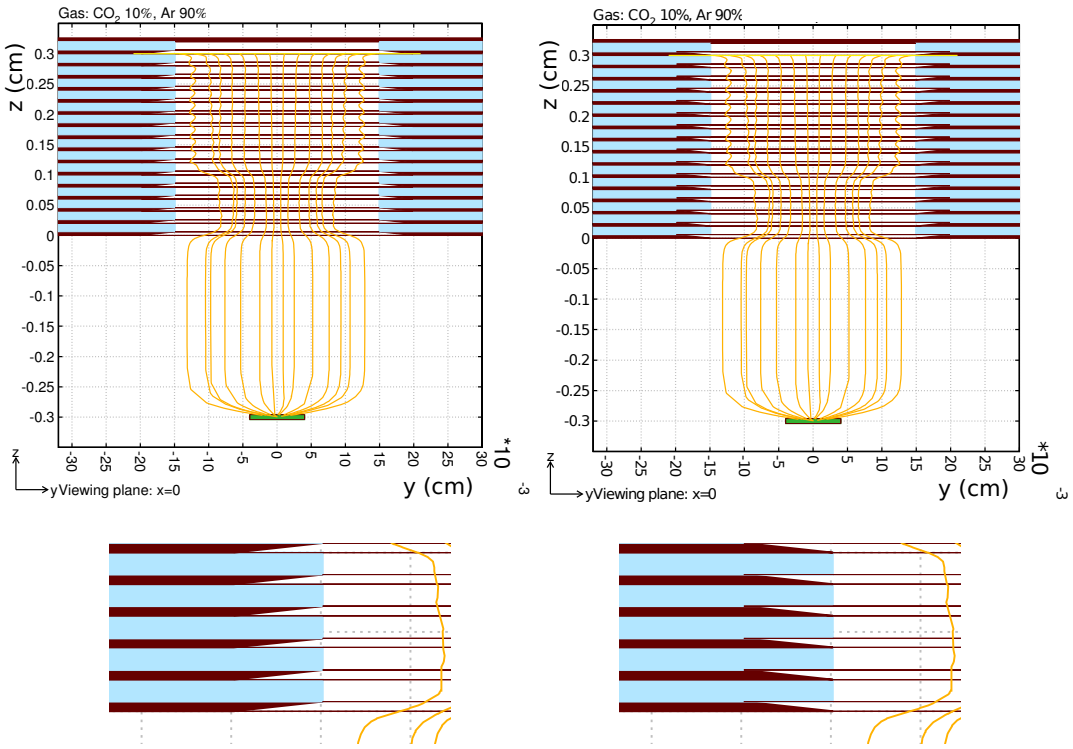

Figure VI.11.: *Left: Garfield simulation of electron drift lines of setup 1 (top) and close-up of the cone-shape (bottom). Lead layers are visualized in brown and kapton foils in blue color. The wire plane is represented by a green box.*
Right: Garfield simulation of electron drift lines of setup 2 (top) and close-up of the cone-shape (bottom).
The drift lines for setup 1 and setup 2 do not differ.

generated within a range of 25 µm from the solid will probably be re-absorbed regardless of the z-position at generation.

VI.3.5. Garfield sensitivity map

A feature of Garfield is the microscopic simulation of the movement of an electron through gas. If the procedure *DRIFT_MICROSCOPIC_ELECTRONS* is called, the electron location will be tracked for n collisions, with n specifying the *MC*-collision parameter. The *MC*-collision parameter of this simulation is set to 1000. Each collision is classified into elastic, inelastic, attached or ionized. This classification can be used for further analysis.
The goal of this simulation is to get an understanding of the behavior of ionized electrons

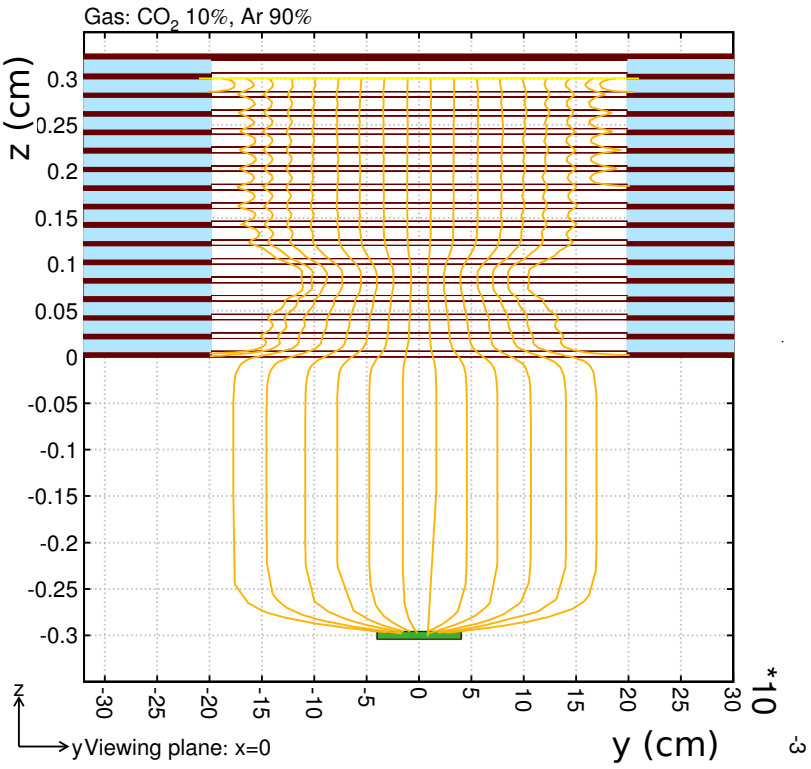

Figure VI.12.: *Garfield simulation of electron drift lines from a track for a tube-shaped hole. The majority of drift lines will reach the wire plane. Only drift lines within a range of 25 µm from the solid end before reaching the wire plane.*

inside a hole. Therefore, a set amount of microscopic electrons is generated throughout the hole and hits on the wire plane are counted. The obtained result is the sensitivity map of figure VI.13.

It shows that only in the lowest centered part of a hole, relatively high sensitivities of 50 % can be achieved. Away from this center, sensitivity quickly decreases and reaches values of only 5 % in the very corners of a hole.

However, this does not mean that the majority of events cannot be detected. The simulated microscopic electrons are comparable with secondary electrons in reality. If a photon is converted into an electron leaving the lead and passing a distance of 400 µm in the hole, the electron will ionize about four secondary electrons around its point of interaction [PPB10]. Therefore, there are always four chances for an event to be detected, with different probabilities depending on the point of interaction inside the hole.

Regarding the sensitivity distribution, the idea comes up that the stacking of 16 layers is not fully necessary or maybe even not optimal. According to [Got10], the mean exit angle of electron emission is 45 °. Since the general sensitivity of a converter with fewer layers should not dramatically differ, a converter consisting of less layers will have big advantages manufacturing-wise.

There is an additional argument which hints to the idea of assembling less than 16 layers. Previously, an increase of the thickness of the kapton foil and a decrease of the hole diameter have been discussed. In fact, this will result in longer and thinner holes, which again affect the electric field, and therefore the drift lines inside the hole. Such holes might cause more absorption and less detection on the wires. A reduction of assembled layers could help optimizing sensitivity.

Besides, it might be helpful to change and adjust the cascading voltage applied on the lead layers to obtain the maximum number of detectable events. First, this can be done by additional simulations or in future even experimentally with the help of the converter test device (see chapter VIII).

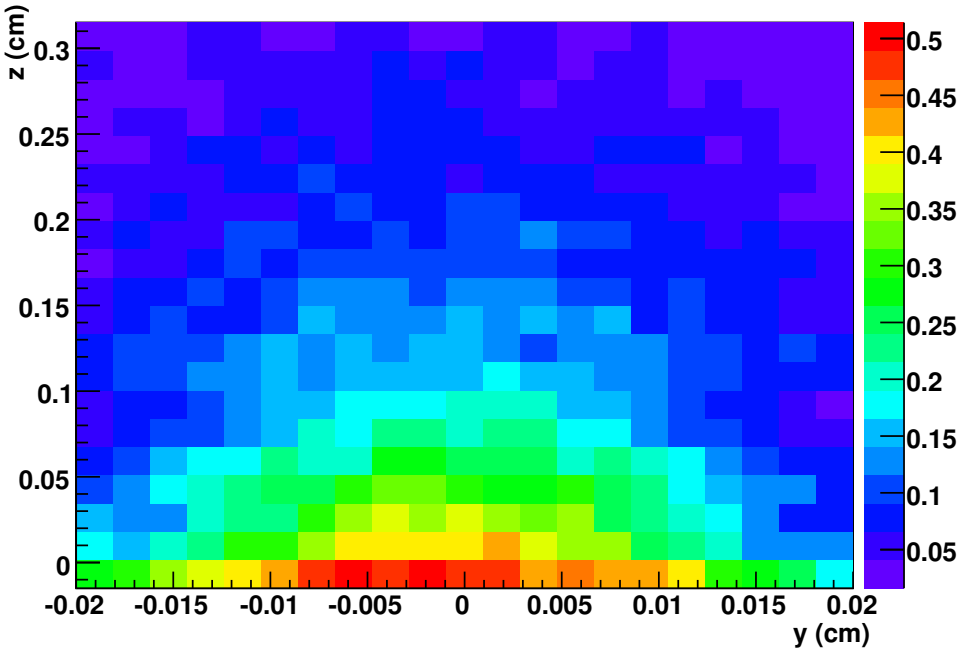

Figure VI.13.: *Sensitivity map calculated by simulations with Garfield [Ver11]. The ranges of axes of abscissae and ordinate restrict one hole (⌀400 µm). Relatively high sensitivities can only be achieved in the lowest centered part. Away from this center, sensitivity quickly decreases.*

VI.4. Present status

This chapter discussed many parameters regarding the geometry of a converter. To get an overview of the possible current realizations, some results are summarized.
The modified code predicts a sensitivity of 6.9 % for the quadHIDAC. This includes displaced 400 µm-holes at a pitch of 500 µm in both directions. Currently, it would be possible to rebuild the quadHIDAC with an optimized hole geometry. This means that the holes would still be drilled, but with an improved drilling technique. Instead of 500 µm-pitches in both directions, a triangular geometry is suggested consisting of a hole distance of 500 µm in the one, but only 433 µm in the other direction. This results in a sensitivity of 8.2 %, which is a relative increase of 18.8 %.
Assuming it is possible to make use of an alternative technique, such as etching, the bridge between two holes could be optimized from 100 µm to 50 µm. Including a triangular geometry, this potential quadHIDAC would result in a sensitivity of 9.0 %, which is an increase of 30.4 % compared to the present quadHIDAC.
Since the influence of a thicker kapton foil is questionable, it remains unsettled whether it is realistic to say that an additional increase of the thickness of the kapton foil will result in sensitivities around 10.0 % for both mentioned improvements, which corresponds to a relative enhancement of 45.0 %.

VII

Read Out of Single quadHIDAC Modules

The quadHIDAC, as it is standing in the European Institute for Molecular Imaging (EIMI), has been running reliably for many years providing satisfying research results. However, recently, it was necessary to remove several modules from the scanner because they lacked sensitivity in comparison to proper operating modules or because they broke down completely. It is already known that disturbances of operation are caused by aging effects. For example, over the time, ionized molecules of the gas build up polymers. These polymerisation crystals will then stick to cathode pads, anode wires, and even block holes of the converter [Got10]. Nevertheless, there might be some other aspects as well e.g. broken wires.
Due to the lack of support and service, future operation will be problematic. On this account, an attempt was started to repair the incorrectly operating modules.
Consequently, the removed quadHIDAC modules have to be evaluated before and after the repair. For systematic error estimation, it is important to see in which way the incorrectly operating modules are running to learn about the appearing defects. Furthermore, there is a major interest in generally understanding the operational scheme of the quadHIDAC modules because this has not been fully documented. In addition, a comparison between previous modules and repaired ones on a reliable basis is desirable.
The difficulty was to generate an appropriate setup which is able to hold and read out single quadHIDAC modules because, up to this point, quadHIDAC modules have only been operating in the PET scanner environment itself. In cooperation with the EIMI, it was decided to design and install a module carrier system [Bol10] in the PET-laboratory of the institute for nuclear physics Muenster which is able to hold any size of quadHIDAC modules. The advantage of this laboratory is that it already offers a complete read out procedure which has been priorly used for measurements with prototypes of

MSPET-chambers [Ver10].
Unfortunately, it is not only the operational scheme of the modules which is not understood, but also the read out code of the quadHIDAC scanner that is inaccessible. Therefore, it was mandatory for the success of the project to develop a reliably working code which is able to handle the collected data. This will be discussed in more detail in section VII.3.

VII.1. Setup

The module carrier system is designed as a frame of stainless steel which can potentially hold two modules at a time. At a height corresponding to the middle of the modules, there is an adapter leading the induced charges from the pads onto LEMO connectors. The signals are then pre-amplified via charge sensitive PNG CATSA devices and shaped by PNG MA8000 main amplifiers. The digitalization process of the signals is carried out by a peak sensing analog-digital-converter (CAEN V785N). This entire procedure of data acquisition can be controlled via C-based code implemented by [Pie08]. It can be modulated to either record one or two dimensional event information. Figure VII.1 shows the just mentioned setup for the measurements.

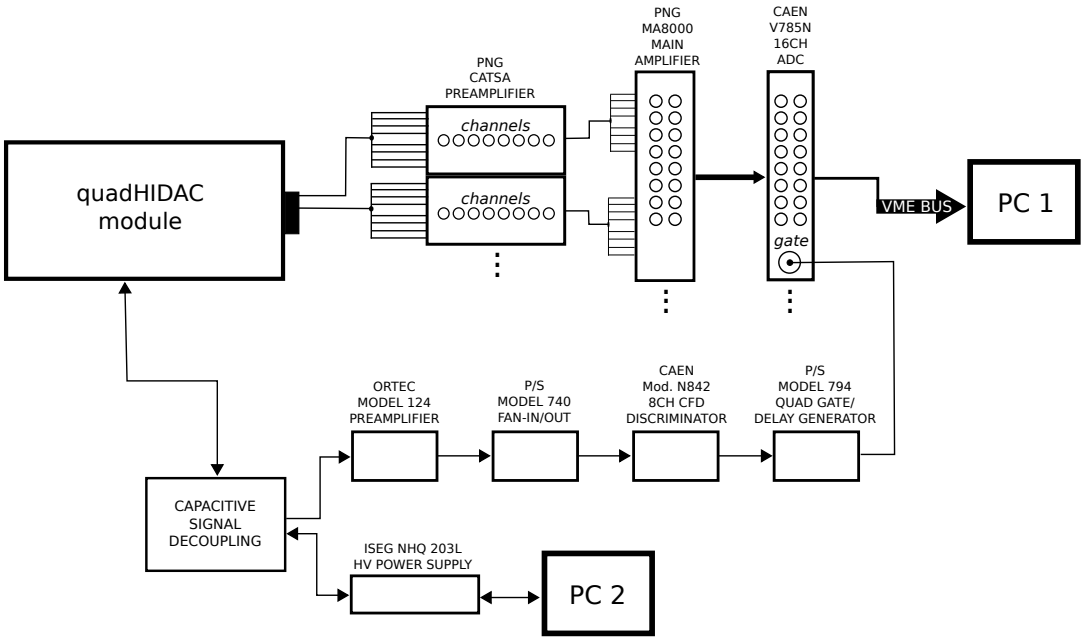

Figure VII.1.: *Setup for the measurements with single quadHIDAC modules outside of the PET scanner environment.*

In general, the measurements were carried out with one of ^{22}Na source with activities of 350 kBq[1] and 47 kBq, respectively. The source was mounted in the center of the carrier system movable with the help of a linear stage. In operation, the source was shifted to a distance of a few millimeter from the module concentrating irradiation to the center. It is to mention that the count rates for the single modules, which were obtained with this setup, were an order of magnitude smaller than the count rates measured in the quadHIDAC environment. Probable reasons are the PNG CATSA and ORTEC pre-amplifiers since these were actually developed for solid state detectors and are not well suited for this application.

VII.2. Read out logic

Each quadHIDAC module holds a plane of 144 700 µm-cathode pads arranged in 300 µm distance determining the x- position. The number of cathode pads determining the y-position varies with the length of the module from 70 to 140.
To minimize the required number of read out channels, the read out is performed block-wise. There are 12 blocks per dimension each holding the integrated charge over 12 pads. In addition, the 144 pads are divided into 24 groups. For the y-read out, these numbers deviate and are often smaller than the typical number. The adjacent even-numbered pads of a group make up blocks 1 to 6 which allows to determine the approximate region of an event. Blocks 7 to 12 consist of one uneven-numbered pad of each group which allows to locate the exact pad on which the event took place. The scheme of the read out logic is depicted in figure VII.2.

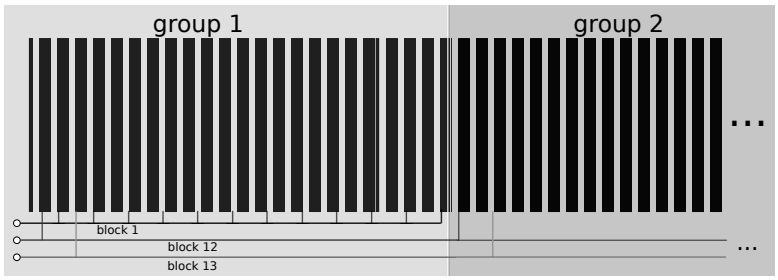

Figure VII.2.: *The read out logic consists of groups of 24 pads arranged in blocks of 12 to minimize the number of required read out channels.*

[1] 1 Bq=1 Becquerel=1 per second

VII.3. Read out code

The first analysis step is the determination of the baseline out of the raw data including its subtraction. The corrected data will then be converted into ROOT-tree format to be analyzed with the main analysis code *quadHIDAC_analysis.c*. This main program holds all necessary features to obtain a full analysis. The ROOT-tree format has the advantage that the event-per-event analysis is easy to handle.
The first part of the program sorts the corrected ADC values of one event in x- and y- data classifying the already mentioned blocks of 12 entries each. Blocks 1 to 6 of x- and y- data are subsequently scanned to determine the region of maximal charge deposition ($\text{block}_i = \text{Q}_{\text{max},1}$).
The same procedure is applied to blocks 7 to 12 ($\text{block}_j = \text{Q}_{\text{max},2}$). According to the fact that the pads of blocks 7 to 12 are positioned at a distance of 12 mm and the baseline has already been subtracted, it is assumed that the integrated value given by block_j equals the charge deposited on the pad which belongs to the group of 24 including the previously determined block_i. Once the blocks indicating the region and the position of maximal charge deposition are defined, an algorithm will calculate the corresponding x- and y- coordinates determining the 2D position of the detected event with a resolution of one pad width. In the following, these coordinates are used for reconstruction purposes.
The second part of the program performs calculations based on the event coordinates and its charges, and provides several graphical outputs in the end. The outputs include event maps, histograms of x- and y- data, the PRF and its profile, a variety of visualized displacement calculations, and the theoretical Mathieson formula as a reference.

VII.4. Analysis

The very first analysis step will cut for $\text{Q}_{\text{max},1}$- values lower than 100 mV and higher than 4000 mV because these values are considered to be either noise or overflows. The cuts for $\text{Q}_{\text{max},2}$ are at lowest 33 mV and at highest 1333 mV which is 1/3 of the $\text{Q}_{\text{max},1}$ -cuts (argumentation see below).
An analysis step to check the quality of the recorded events regarding the maximal charges is the generation of a two dimensional histogram of maximum charges. The axis of abscissae holds $\text{Q}_{\text{max},1}$, whereas the axis of ordinates $\text{Q}_{\text{max},2}$. An example of this plot is given in figure VII.3.
The 2D histogram is an example of a successful measurement. There are no obvi-

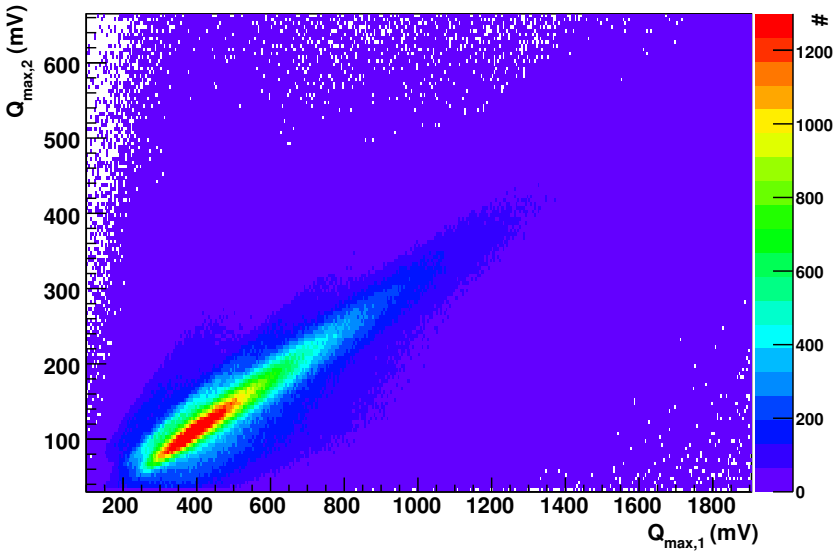

Figure VII.3.: *Two dimensional histogram with maximum charge of the first 6 blocks $Q_{max,1}$ plotted versus maximum charge of the second set of blocks $Q_{max,2}$. From this plot, one obtains a first evaluation of the quality of the events. Settings of measurement #270810-7:*

U (anode)	*2000 V*
U (cathode)	*-3000 V*
trigger threshold	*8 mV*

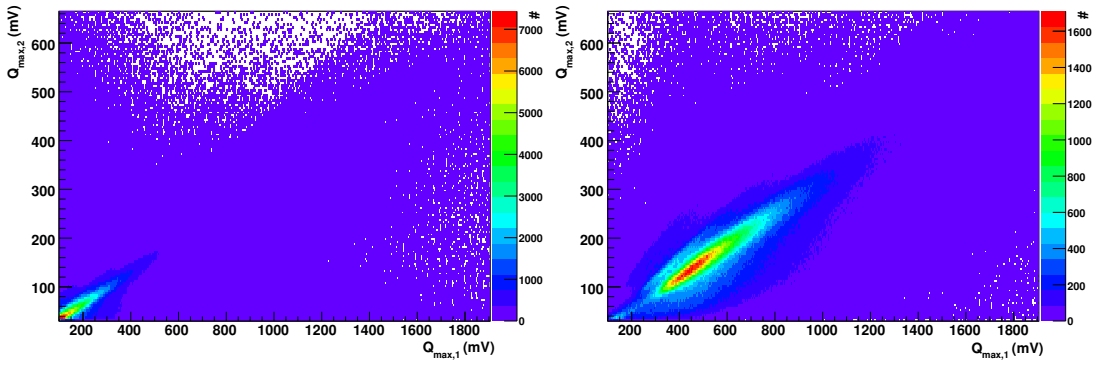

Figure VII.4.: *These plots are examples of events of bad quality due to inappropriate voltage and trigger settings. Settings of measurements:*

Left:	*#270810-4*	*Right:*	*#270810-3*
U (anode)	*2000 V*	*U (anode)*	*1950 V*
U (cathode)	*-3000 V*	*U (cathode)*	*-2970 V*
trigger threshold	*0 mV*	*trigger threshold*	*10 mV*

ous hot spots or irregularities. The majority of events is linearly located between $Q_{max,1}$= (250 - 750) mV and $Q_{max,2}$= (60 - 240) mV. The linear relationship hints to the fact that the pad response of the module is rather uniformly distributed. Additionally, $Q_{max,2}$ is approximately 1/3 of $Q_{max,1}$. The reason for that is the integration over the 12 charges of one block. $Q_{max,1}$ holds significant charges of several pads due to a broadly induced charge distribution caused by the avalanche.
The 2D histograms in figure VII.4 are examples for bad results regarding charge quality of the events. The charges of the left plot are too focused on small charges and the charges of the right plot show an irregular behavior for small $Q_{max,1}$- and $Q_{max,2}$-values and, in addition, a broader distribution compared to the plot in figure VII.3 with the majority of events for $Q_{max,1}$ between 200 mV and 800 mV and $Q_{max,2}$ between 33 mV and 280 mV. The reason for this are inappropriate voltage and trigger settings or in some cases even disfunctional modules.

After a statement about the quality of the charges of the events is possible, the coordinates-reconstruction-algorithm will generate outputs as shown in figure VII.5. These examples show a 1D reconstruction of measurement #270810-7 and a 2D reconstruction of measurement #151010-3. For both measurements, the source was positioned close to the center of the quadHIDAC module.

Regarding these reconstruction results, one can say that the coordinates-reconstruction-algorithm is performing well. The source is well seen in 1D and 2D respectively by the high amount of events concentrated at 1D: x = (100 mm,150 mm) and 2D: x = (110 mm,150 mm), y = (50 mm,80 mm). The reliability of the code has been tested successfully on several measurements of variable sources, source positions, measurement times, and modules. This success in developing a reliable working read out code for single quadHIDAC modules will now allow the evaluation and comparison of operating, broken, and repaired quadHIDAC modules.

In addition to the pad-wise reconstruction of the event distribution, it is possible to calculate the displacement of the charge distribution on the pads as introduced in section V.3. The idea is to improve the spatial resolution of the reconstruction. Since the read out code of the quadHIDAC scanner is inaccessible, it is unknown whether the quadHIDAC scanner uses this kind of reconstruction algorithm or whether the reconstruction is just based on a resolution of one pad width.
The basic reconstruction of figure VII.5 (top), including the values for the displacements

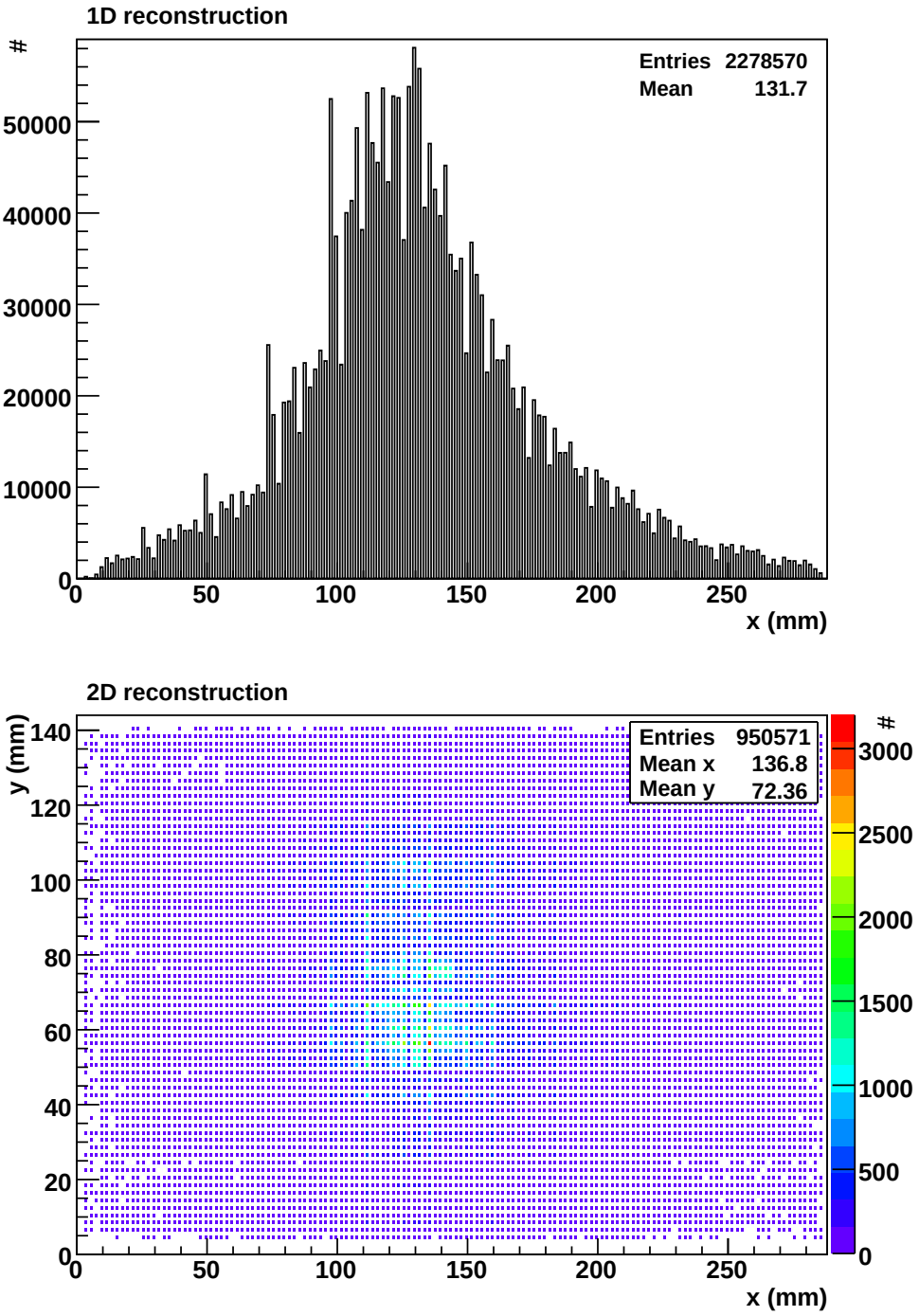

Figure VII.5.: *1D histogram of the reconstructed x-positions and 2D histogram of the reconstructed x- and y-positions.*

Top:	*#270810-7*	*Bottom:*	*#151010-3*
U (anode)	*2000 V*	*U (anode)*	*2100 V*
U (cathode)	*-3000 V*	*U (cathode)*	*-3000 V*
trigger threshold	*8 mV*	*trigger threshold*	*8 mV*

of the events, is shown in figure VII.6 (left). On the right side, there is the overall distribution of calculated displacements. The displacements' distribution is approximately uniformly distributed over the entire displacement range of (-1.0 mm,1.0 mm) being rather planar, which is very satisfying because it corresponds to the statistical probabilities.

Alternatively, the weighted displacement function[2] and its displacements have been applied. The reconstruction with the help of the weighted displacement function (shown in figure VII.7 (left)) seems more fluctuating compared to the unweighted displacement function. This is underlined by the consideration of the calculated displacements (figure VII.7 (right)) showing a tendency to calculate displacements not too far from the center of the pad.

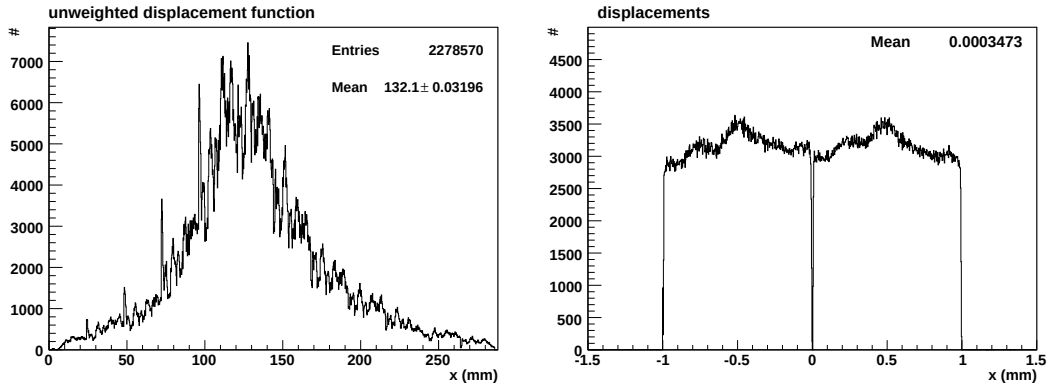

Figure VII.6.: *Left: Reconstruction with the help of the unweighted displacement function.*
Right: Approximately uniform distribution of the calculated displacements of the events.

The possible improvement of the spatial resolution due to the weighted displacement function cannot be underlined at this point. Indeed, there is a difference of the mean values for weighted and unweighted displacement functions of about (0.10 ± 0.05) mm, but considering the rather round shape of the displacements' plot in figure VII.7 (right), this deviation is more likely caused by the biased calculation than by an improvement in spatial resolution.

It is to mention that the entire experimental setup is, in general, not suited for resolution measurements since it is actually impossible to collimate an appropriate source somehow to the quality of a particle beam.

[2]Determination of the standard deviation σ see section VII.5.

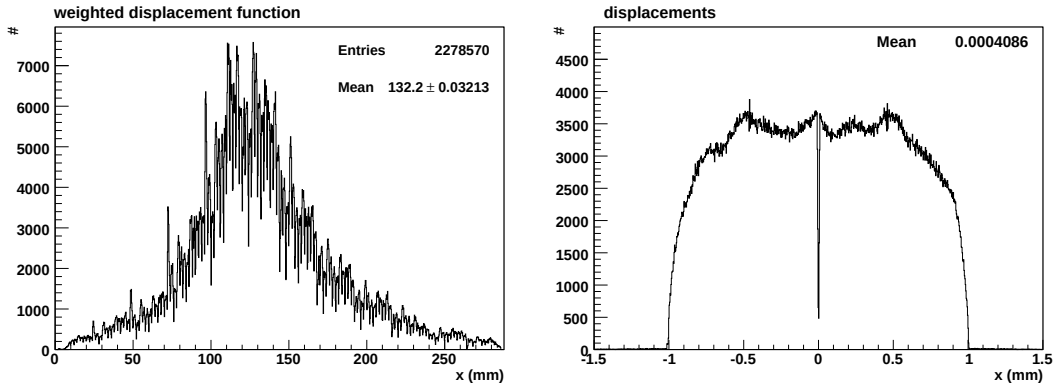

Figure VII.7.: *Left: Reconstruction with the help of the weighted displacement function.*
Right: The distribution of the calculated displacements of the events shows a rather round shape.

In conclusion, it can be stated that if a displacement calculation for the read out and evaluation of the quadHIDAC modules was necessary, it would be recommended to use the unweighted displacement function in the analysis. The results obtained with the center of gravity method, the Lorentzian and Parabolic curve fitting are either similar or even worse than the results for the weighted displacement function.

VII.5. Pad response function

Considering equation V.22, the weighted displacement function can only be applied if a suitable standard deviation σ is found. The determination of the standard deviation from the PRF is done by plotting the unweighted displacement of the pad with maximum charge against the quotient of one of the three charges participating to the calculation of the displacement and the sum of the charges of the three participating pads. This *pad response function plot* (PRF-plot) is shown in figure VII.8.
The theoretical curve represented by the black line can be calculated with equation V.15. In this case, experimental data and theory are disagreeing (as will be discussed in subsection VII.5.1). Besides, the PRF-plot spreads widely reaching values up to 0.33, which occurs if the induced charge has been equally distributed over three pads. This is the case when the avalanche multiplication is not fully taken up by just one, but by several wires. This happens if an electron crosses the gaseous volume of a chamber in a wide angle with the perpendicular of the wire plane.
The determination of the standard deviation σ is done with the help of the profile of

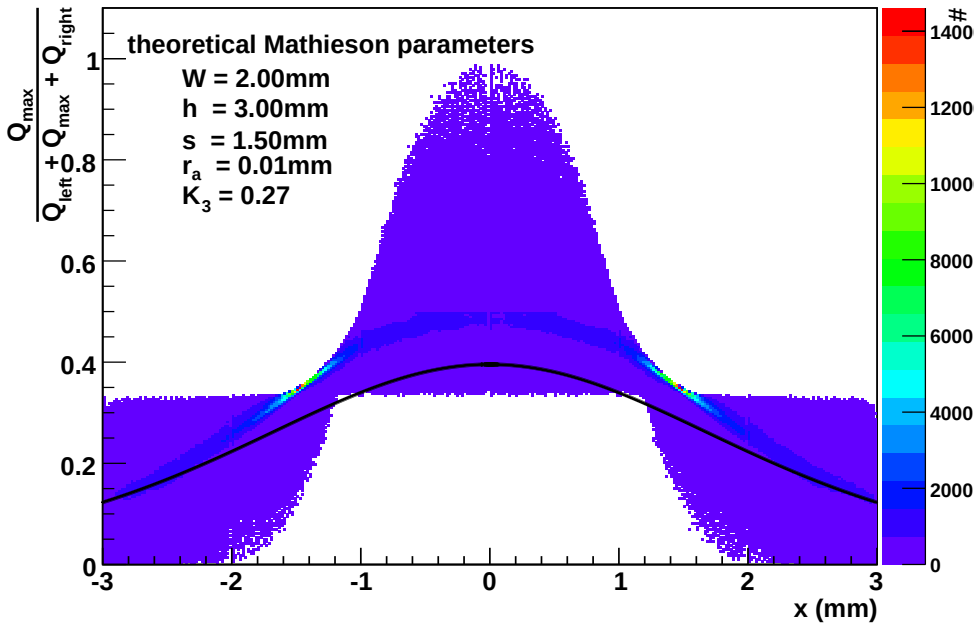

Figure VII.8.: *Pad response function plot (PRF-plot) and theoretical Mathieson formula indicated by the black line. The theoretical run and the experimental data disagree.*

the PRF, which is shown in figure VII.9. The profile consists of the averages of each bin of the PRF-plot. The application of a Gaussian fit to the profile determines σ to (1.631 ± 0.001) mm.

Unfortunately, the Gaussian distribution only suits well to the non-centered charges due to the odd and rather straight behavior of the average values at x = (-1.2 mm,1.2 mm). Therefore, the χ^2/NDF is rather high. However, for the determination of σ, the x-position of the maximum and the decline of the Gaussian are significant, and since these parameters suit well, the standard deviation obtained with the help of the Gaussian fit could be determined with a low uncertainty.

VII.5.1. Mathieson PRF

The PRF determines the fraction of the total cathode signal induced on the pad as a function of the distance between the center of the pad and the avalanche position. In figure VII.8, there is no agreement between the theoretical Mathieson PRF (equation V.15) and the experimental data. The parameters which were used for the calculation of the PRF are indicated in the plot. The fixed parameters h (anode-cathode dis-

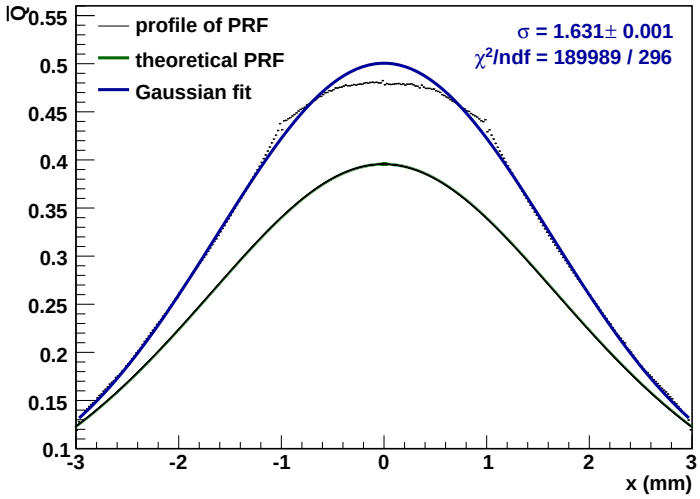

Figure VII.9.: *The averages of the values from the PRF-plot* $\bar{Q} = \sum_{i=1}^{n} \frac{1}{n} \left(\frac{Q_{max}}{Q_{left}+Q_{max}+Q_{right}} \right)_i$ *to determine the standard deviation* σ *from a Gaussian fit (blue curve).*

tance: 3.00 mm), s (wire pitch: 1.50 mm), and r_a (wire radius: 0.01 mm) are defined by the chamber's geometry. This should account for the pad width W as well. However, due to the read out logic of the quadHIDAC, the theoretical calculation has to consider two real pads as one calculation pad and add the two gap distances of 300 µm each. Therefore, the pad width W is here set to 2.0 mm, and neither 0.7 mm, nor 1.0 mm (differences shown in figure VII.11 (left)).

Another occurrent problem when calculating the PRF is the determination of K_3. K_3 can generally be obtained from figure V.3 in dependence of the chamber's geometry. For the quadHIDAC geometry, h/s equals 2.0 and r_a/s is 6.67×10^{-3}. Unfortunately, this geometry has not been recorded in literature, but there are values for $r_a/s = 5.25 \times 10^{-3}$ and $r_a/s = 7.50 \times 10^{-3}$. Considering figure VII.10, K_3 should lie in between 0.26 and 0.29 in the case of the quadHIDAC geometry.

The influence of the pad width W and the parameter K_3 on the developing of the PRF is presented in figure VII.11. Varying the pad width W, the maximum of the PRF varies up to a factor of 50 %, whereas with variations of K_3 the deviations are rather small. Even if assuming a relative error of 60 % on the estimation of K_3, which corresponds to an absolute error of 0.16, the PRF's range will maximally vary by ± 6 %. Therefore, a wrong estimation of K_3 cannot cause the observed deviation between experimental data and theory in figure VII.8.

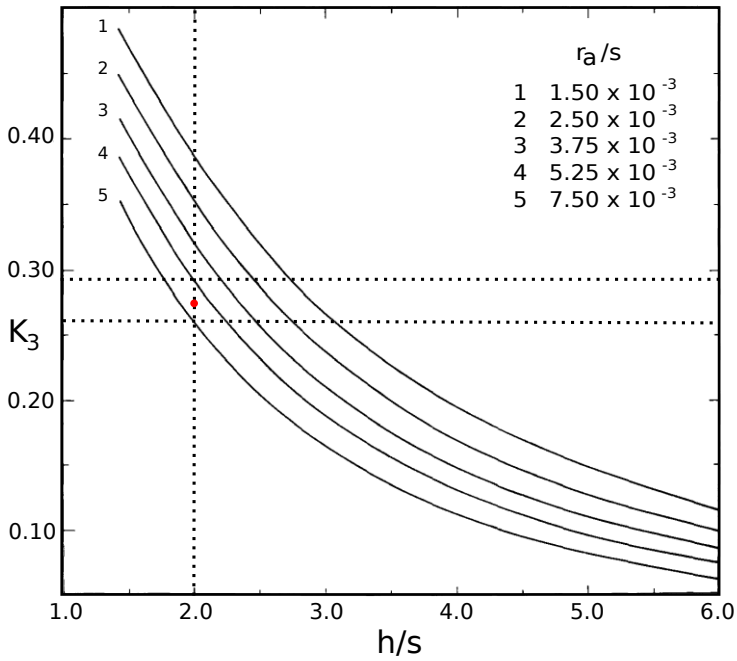

Figure VII.10.: *K_3 in dependence of the chamber geometry. The K_3- value according to the quadHIDAC geometry of $K_3 = 0.27$ is marked red [Mat84].*

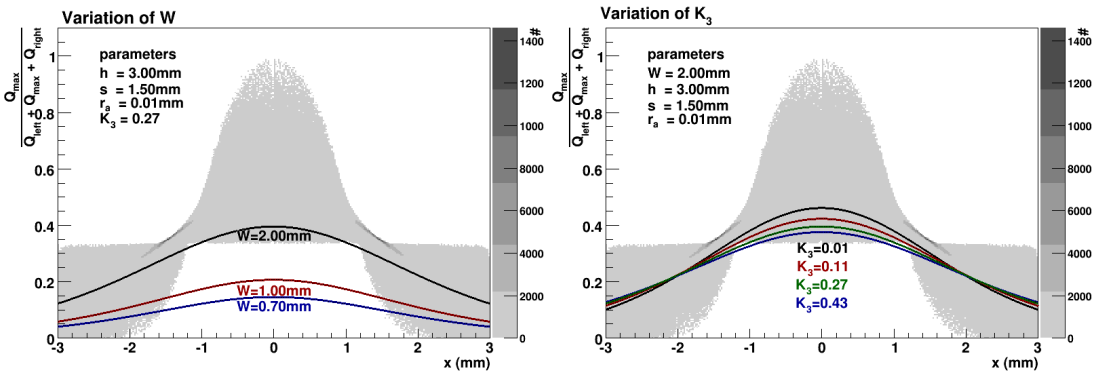

Figure VII.11.: *Left: The experimental data is compared to the PRF of varying parameter W. The maximums of the theoretical PRFs vary up to 50 %.*

Right: The experimental data is compared to the PRF of varying parameter K_3. In this case, the deviations for the PRFs are rather small compared to the deviations for the width W.

VII.5.2. Simulation of the PRF

It has already been mentioned that the profile of the PRF in figure VII.9 does not overall suit a Gaussian distribution. To examine this behavior, a suitable simulation was necessary.
The simulation and its analysis were implemented in ROOT. Basically, the code generates Gaussian distributed track positions on the simulated pad geometry where it induces Gaussian distributed charges. The charges are read out pad-wise and saved in ROOT trees. From there on, several analysis steps can be taken. The analysis of this simulation only includes the charges of the uneven-numbered pads, which is due to the quadHIDAC's read out logic.
The converter design of the quadHIDAC has been introduced in section VI.2. The interleaved lead and isolation layers are holding a hole geometry. This geometry is passed on to the pads of the pad plane. For the simulation, the implemented pad geometry can be chosen to either include or exclude the holes. Sections of the potential pad designs are shown in figure VII.12.

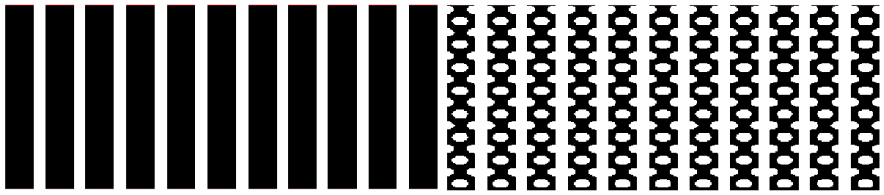

Figure VII.12.: *Left: Pad plane without holes.*
Right: Pad plane holding a hole geometry.

A comparison of the PRFs of 100,000 simulated events is illustrated in figure VII.13. Regarding the pad response, there is absolutely no deviation between a pad geometry including holes compared to a plane one. However, the hole geometry will influence the intensity of the induced signals. The charges of the pads holding holes are only $(63.84 \pm 0.14)\,\%$ of the plane pads.
Additionally, these simulated PRFs show a similar rather odd behavior of the average values at x= (-1.2 mm,1.2 mm). Again, the Gaussian distribution only suits well to the non-centered charges. However, the flattening of the charges around x= 0 mm is not as pronounced for the simulated data as it is for the experimentally obtained data. The correspondence between simulation and experimental data is shown in figure VII.14.
In general, one can state at this point that the theoretical Mathieson formula is not suited to describe the induced charges on the quadHIDAC pads. The conflict arises

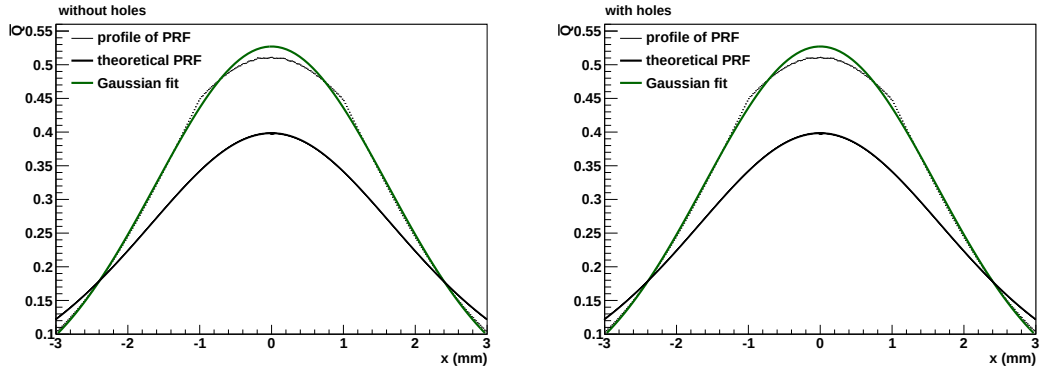

Figure VII.13.: *The profile of the PRF for two simulated pad geometries is shown in addition to the theoretical PRF and a Gaussian fit. There is no deviation between the two profiles.*
Left: The simulated pad geometry consists of plane pads.
Right: The simulated pad geometry includes holes on the pads.

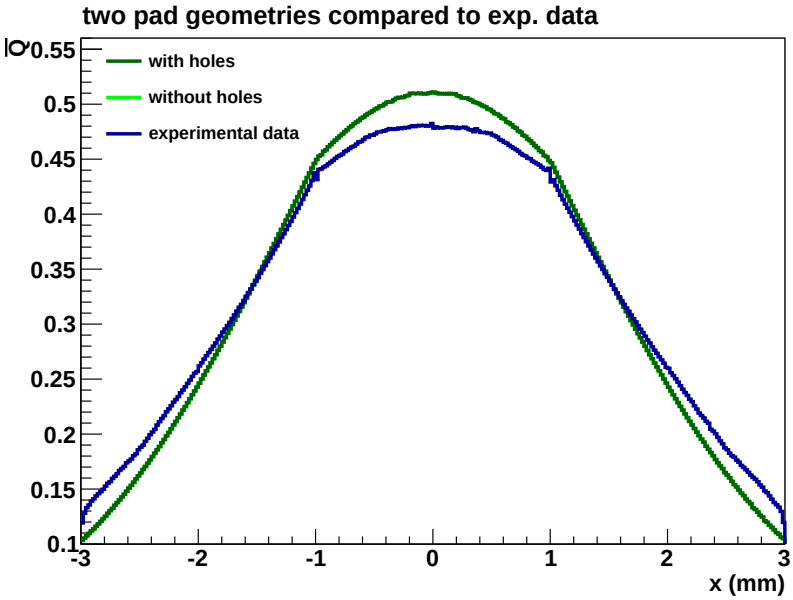

Figure VII.14.: *The two simulated pad geometries are compared to the experimentally obtained data. The shape is similar, but more pronounced for the experimental data.*

from the fact that the read out logic of the quadHIDAC only considers every second pad significantly whereas the Mathieson formula assumes perfect avalanches hitting just one wire inducing perfect signals on adjacent pads.
It has already been mentioned that the pad width of the quadHIDAC geometry is 700 µm holding 300 µm gaps. This width is very uncommon for pad geometries as it is rather small compared to common detector designs. It was assumed that the non-Gaussian distribution might be affected by the pad width, therefore supplemental simulations were run for variable pad widths between 2 mm and 4 mm, where the 2 mm pads represent the pads of the quadHIDAC. The obtained profiles are shown in figure VII.15.

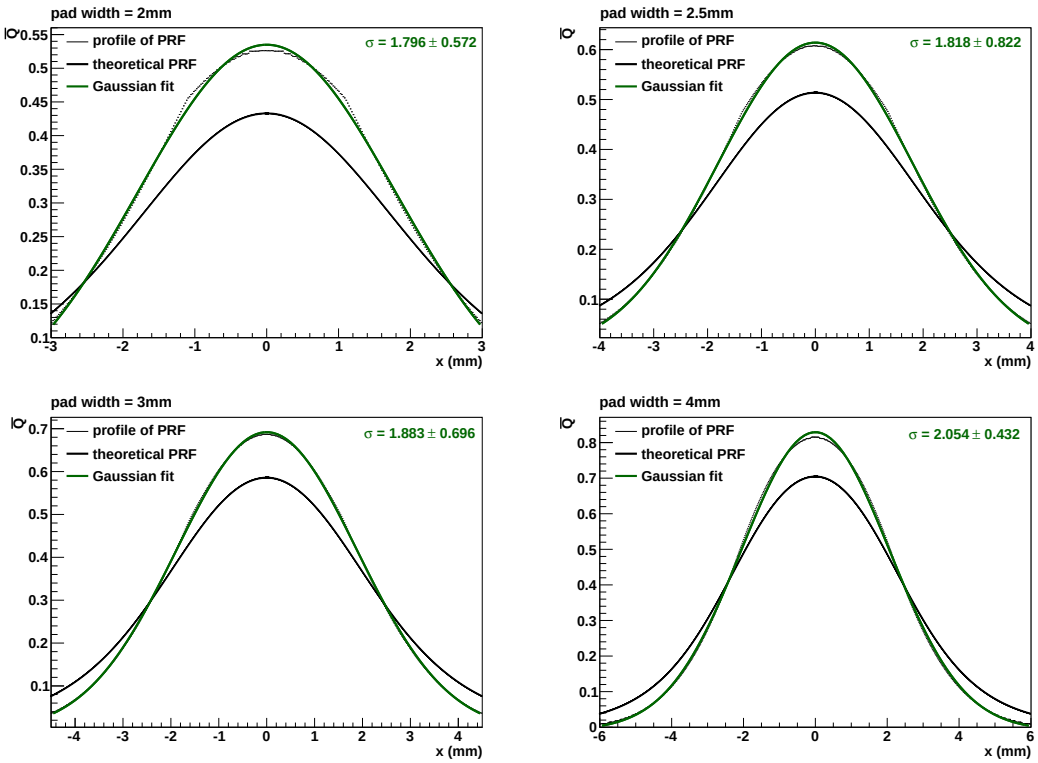

Figure VII.15.: *Simulations of pads of variable widths. Wider pads show a Gaussian distribution for the profile of the PRF whereas with decreasing width deviations occur.*

It is shown that an increase in pad width will result in profiles of the PRF which are in better correspondence with a Gaussian distribution. This states that the quadHIDAC pad width is rather unsuitable. To obtain signals which can easily be read out, it is recommended to design a pad geometry with widths around (3 - 4) mm.

VII.6. Defining the operational range of the quadHIDAC module

If the quadHIDAC module is operating in the scanner environment, there is a voltage of 2000 V applied to the anode and -3000 V to the cathode. It is supplied with a mixture of argon, quenching gas, and diisopropylether. In the PET-laboratory of the institute for nuclear physics, diisopropylether is not available and the module has to operate separated from its common environment. Therefore, it is necessary to define a suitable gas mixture and voltage range.

The PET-laboratory holds argon, CO_2, and C_4H_{10} bottles. A common way to determine a suitable gas mixture is the 'trial and error' method. However, it was observed that the chambers were quite sensitive to the mixtures. To receive reliable results, it was necessary to keep the desired mixture flowing for at least half a day. Due to pressure in time, it was decided to simulate the gas gain for the gas mixtures of interest and decide for a suitable gas mixture based on these simulations.

The gas gain simulations were implemented in Garfield. It was decided to compare three mixtures of argon-CO_2 to the same ratios of argon-C_4H_{10}, which is shown in figure VII.16.

The deviations for the three different mixtures of argon-CO_2 are negligible. For argon-C_4H_{10}, the gain increases with the fraction of the quenching gas. Due to the fact that flow and mixture are not perfectly stable and CO_2 has shown satisfying operation in the past, the gas mixture has been set to a ratio for argon-CO_2 of 9:1.

The evaluation of the quadHIDAC module regarding its operation in argon-CO_2 was done by using an X-ray source. The X-ray tube consists of an Ag-cathode delivering a bremsstrahlung spectrum of 3 to 10 keV [Bau05]. To keep the count rate on a manageable level, a 3 mm collimator has been inserted into the X-ray output tube for the measurements. The HV power supply for the measurement was an iseg NHQ 204M device for the cathode and an iseg NHQ 203L for the anode, the present anode current was determined with an HV isolated current meter (Type: A310), and the frequency was read out by an oscilloscope. Figure VII.17 shows the applied voltage depending on the anode current and count rate. The optimal operational range can thereof be deduced to lie between 2000 V and 2200 V. A further increase of voltage will come along with a higher probability for tripping due to an increased anode current.

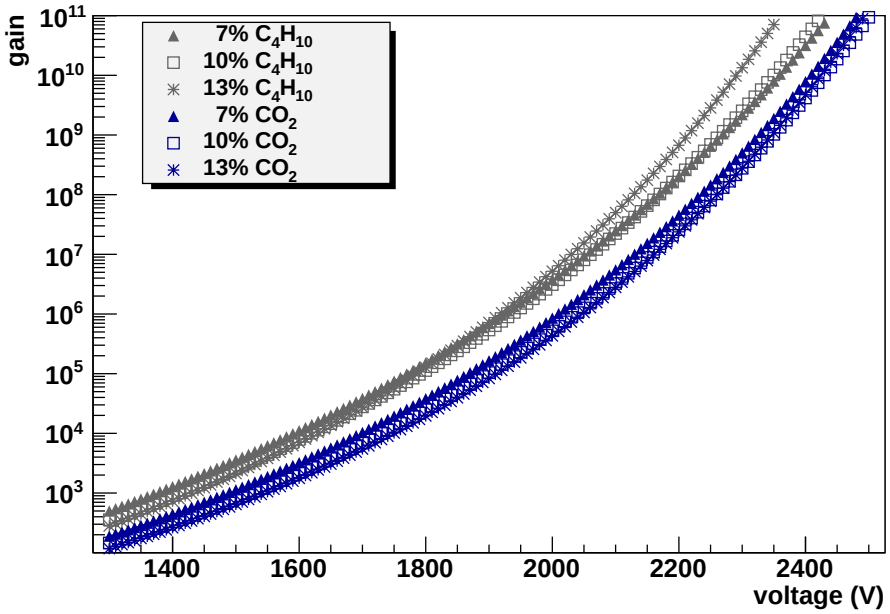

Figure VII.16.: *Gas gain results obtained from simulations with Garfield for three different mixtures of argon-CO_2 and argon-C_4H_{10} respectively. The deviations for the argon-CO_2 mixtures are negligible. For argon-C_4H_{10}, the gain increases with the fraction of the quenching gas.*

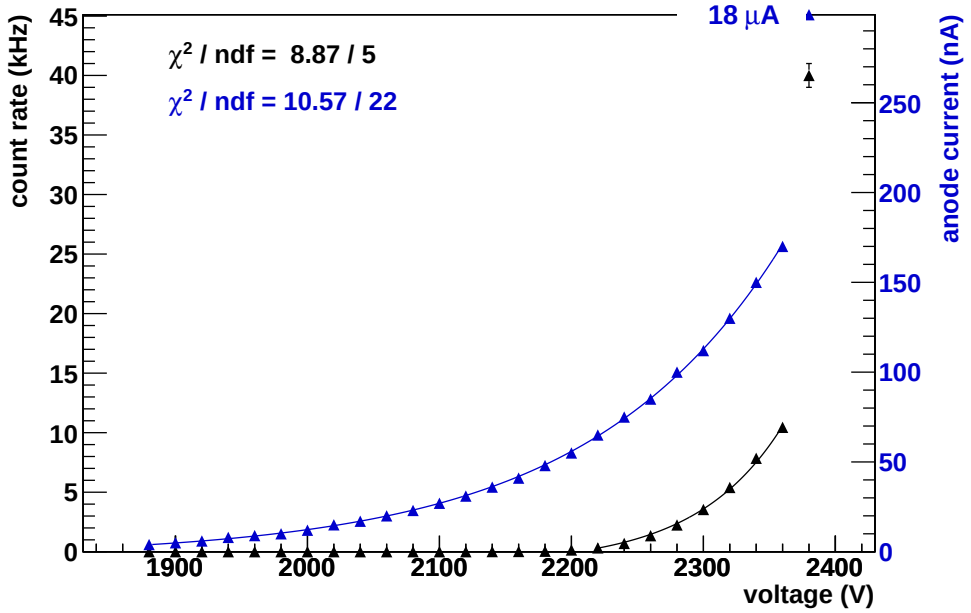

Figure VII.17.: *Relations of applied voltage and count rate respectively applied voltage and anode current for the measurements with the X-ray source. At 2380 V, the chamber trips.*

VII.7. Recapitulatory annotations

The main conclusion of this chapter to be drawn is that the setup for the measurements in combination with the analysis works well. However, due to the deviations regarding the count rates obtained with this setup in comparison to the quadHIDAC environment, it is not possible to make a clear appraisal for the repaired modules. This means that it is not assessable whether the repaired modules will operate in the same way as original modules in the quadHIDAC do. This can only be checked by installing the module in the quadHIDAC scanner.

However, the measurements in the PET-laboratory are suitable to compare between broken and repaired module and one can make a proportionate estimation available. The setup is able to detect in a simple and fast way disfunctions such as broken wires or occurrent currents when applying voltage to the chamber.

Unfortunately, the procedure to setup a measurement is time consuming since, each time, the module needs to be hooked up in the carrier system, 24 channels have to be connected and the supplying gas should flow through the module for several hours before a realistic statement on the module's quality is possible. If this was done for each potential module, the amount of working hours would be enormous. Therefore, only exclusive modules showing unknown operation in the quadHIDAC environment should be hooked up and analyzed. For modules showing a commonly known disfunction in the quadHIDAC environment, it is suggested to repair immediately and re-install without any extra testing.

VIII

Converter Test Device

The production of a new converter can potentially be done in several ways. Drilling techniques, etching processes, and laser technology are manufacturing techniques which are taken into account. In order to evaluate prototypes of converters of all types, a converter test device setup has been designed and assembled.

VIII.1. Converter test device setup

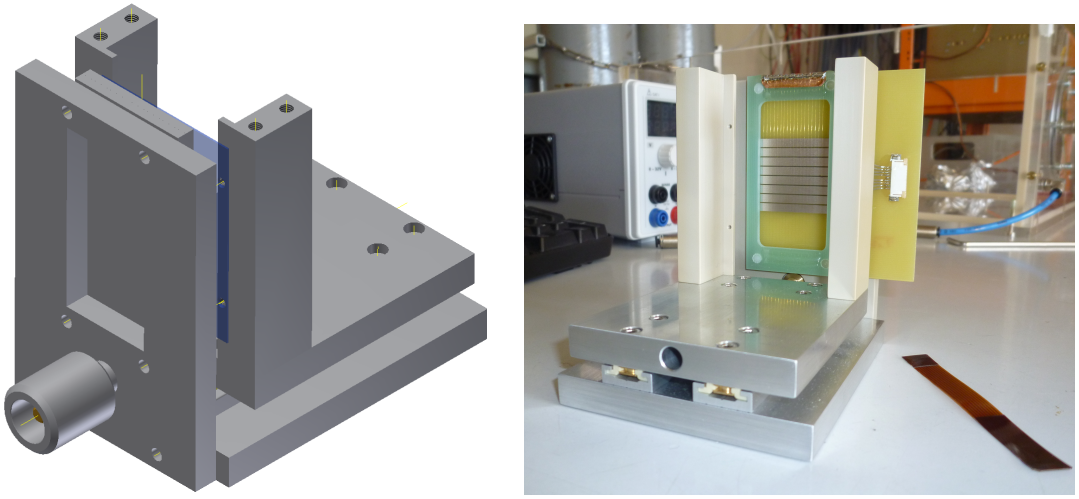

Figure VIII.1.: *Left: Mount of the converter as designed with Autodesk Inventor. Right: Mount before installation in the laboratory.*

The test device setup consists of a box of plastics featuring gas inlet and outlet plus feedthroughs of high voltage supplies and a D-sub connector. The gas outlet is locked

one way by a bubbler to avoid air leaking into the box. The actual measurement setup is placed inside very close to the gas inlet to assure the best possible gas supply. It consists of a wire frame made out of FR4 material positioned at a distance of 3 mm from a cathode pad plane. The wire plane was self-produced with the help of the wire winding machine introduced by [Got10]. The single wires consist of gold plated tungsten with a diameter of 20 µm and hold a tension of 0.5 N at a distance of 1.5 mm from each other. After winding, the wires are glued to the FR4 frame and soldered to an attached piece of copper tape. The cathode pad plane consists of the similar FR4 material. Its pads were added by a combination of resist coating, exposure, and a chemical etching process. The mount for the converter is installed on slides in front of the pad and wire planes allow different converter-wire-frame-spacings, which can be adjusted with a thread bar. This mount can be seen in figure VIII.1, the full measurement setup in figure VIII.2.

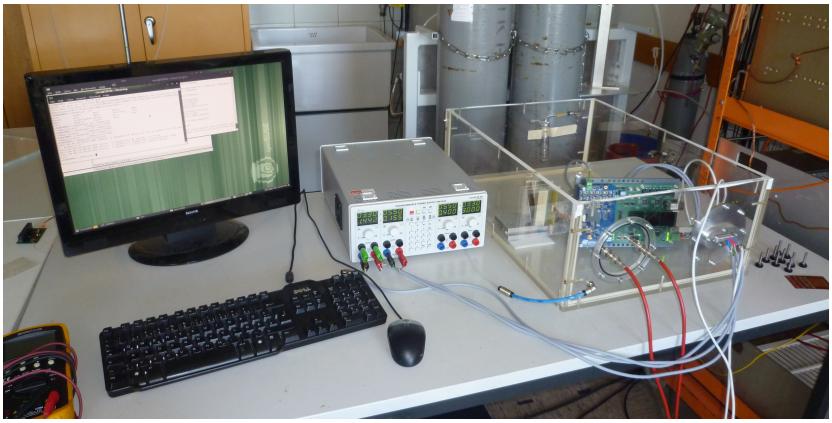

Figure VIII.2.: *The full test device setup installed in the laboratory.*

The read out is done by a *Self-Triggered Pulse Amplification and Digitization asIC* (SPADIC), which has been originally invented as front-end electronics for the planned CBM[1] experiment at FAIR/GSI [Arm10]. The current prototype (revision 0.1) has 8 readout channels each containing a preamplifier/shaper, an ADC, and digital post-processing. With the help of a USB port, the induced charges on the pads can be immediately visualized using the 'hitclient' software which comes along with the SPADIC. The necessary low voltage power supply and the USB port lead in via the D-sub connector are included in the feedthroughs.

The measurement setup is operated in an argon-CO_2 environment. In order to improve

[1] the Compressed Baryonic Matter experiment: `http://www.gsi.de/forschung/fair_experiments/CBM/index_e.html`

the leak tightness, the box of plastics has been sealed with dry adhesive at all edges except for the top. The dry adhesive consists of the components ARALDIT AW 116 and the hardener HV 953 U, which are known for low gas emission properties. The top part of the box is covered with commercially available window seal. Gas tests have been performed with an orbisphere at flows between 20 l/h and 30 l/h. The tightness could then be determined to 40 ppm.

VIII.2. Test converter

After completion of the technical setup, the first goal was launching the test device to prove it is a working concept. For this purpose, we built a test converter consisting of four layers of bronze (60 µm each) and five layers of kapton foil (140 µm each) glued with the already mentioned dry adhesive.

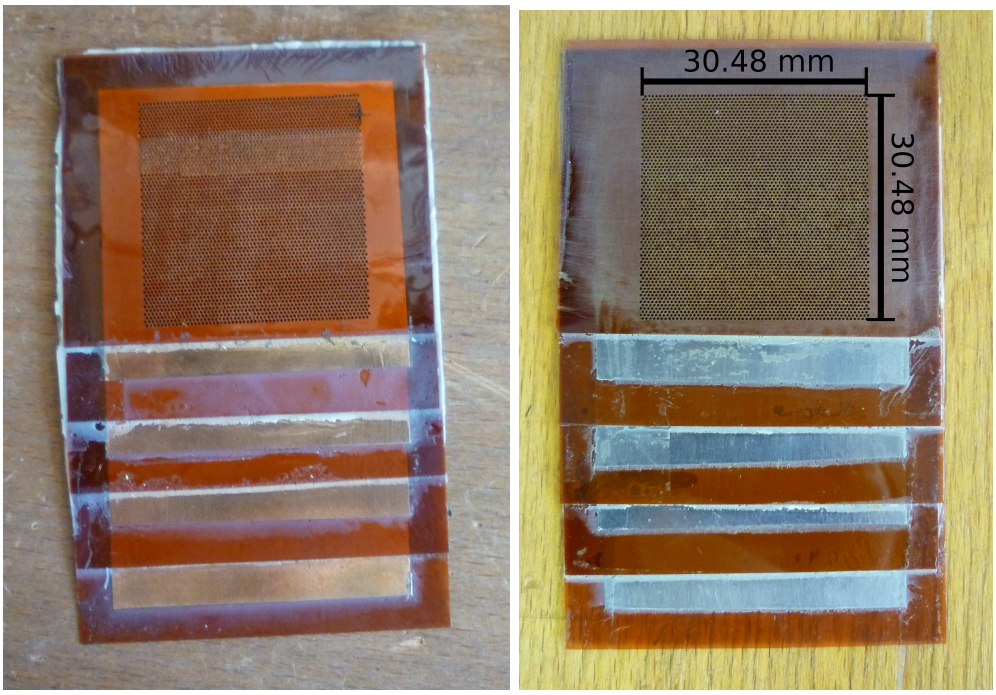

Figure VIII.3.: *Left: The first test converter to adjust the converter test device setup is made out of bronze and kapton foil and was drilled with 5,000 rpm in the university workshop.*
Right: The second converter is made out of lead and kapton foil and was drilled with 100,000 rpm in the CERN workshop.

While age hardening, the converter was squeezed in a molding press. The holes with a diameter of 400 µm were drilled in the university workshop. The drill was able to handle

5,000 rpm[2]. To minimize the probability of broken and stuck drill bits, which can lead to through connections of the converter, the drill bit was replaced every 600 holes. The step size of the machine has been programmed to 0.508 mm with a chosen pattern of 60×60 holes. Therefore, an active area of approximately $(30.48\,\text{mm})^2$ was obtained (see figure VIII.3 (left)). A second test converter was built the same way out of lead (55 µm each) and kapton foil. It was drilled at CERN with a drill handling 100,000 rpm (see figure VIII.3 (right)), which resulted in holes of much higher quality.

VIII.3. Commissioning

VIII.3.1. Voltage tests

In order to evaluate the quality of the converter test device and its components, voltage tests were made. To check for signals, the SPADIC was connected to the pad plane and the ground of the anode plane was soldered to the SPADIC ground, which drastically reduced the noise showing a perfect test pulse signal. The internal trigger threshold of the SPADIC was set to 110 ADC values on channel 1. At a voltage of 1850 V, signals coming from cosmic radiation could already be measured. Figure VIII.4 shows a screenshot of one of the first cosmic signals detected with the converter test device.

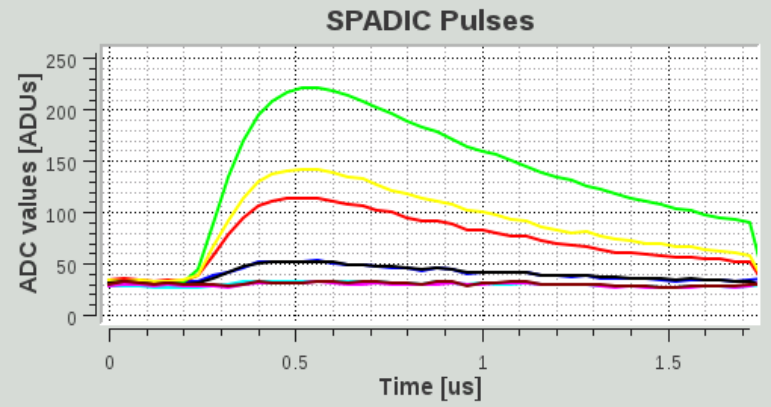

Figure VIII.4.: *This is a screenshot of the hitclient software showing a muon signal measured at a voltage of 1850 V and a trigger threshold of 110 ADC values on channel 1.*

Here, it is remarkable that the signals acquired with the SPADIC and visualized with the hitclient software are smooth and the background noise is small. There are significant charges on three pads (marked by the green, yellow, and red line) which demonstrates

[2] 1 rpm = 1 revolution per minute

that the created avalanche only hits one wire. In a further test, the behavior of the system in presence of a ^{22}Na- source with an activity of 47 kBq was observed.
In this case, the ^{22}Na- source was positioned on the mount which was followed by a remarkable increase in count rate (from 10 Hz to 40 Hz) verifying the assumption that true events can be detected with the help of the converter test device.
So far, there was no converter positioned between source and wire plane. Therefore, the measured count rates are rather low because emitted photons cannot be converted into electrons, and, additionally, the avalanche multiplication is partly disabled due to an inhomogeneous electric field around the wires. The majority of detected signals has its origin in electrons coming directly from the source. A loss of count rate can be observed if the trigger channel is not optimally selected, which means that the source is positioned off-center of the pad selected for triggering.
However, these measurements are successful measurements to proof the concept and hint to reliable results for future converter tests.

VIII.3.2. Expectations for the count rate

To make a statement about the quality of the detection properties of the converter test device, a reference was necessary, and the test device was implemented into Geant4. In this context, the geometry had to be adjusted in the *Detector Construction* class and the ^{22}Na- source generated in the *Primary Generator Action* class. The decay scheme of a ^{22}Na- source is shown in figure VIII.5. In addition to the β^+- decay, a photon with

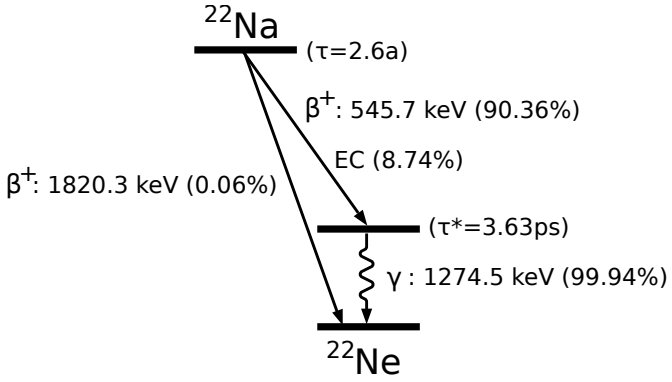

Figure VIII.5.: *Decay scheme of ^{22}Na [NNDC].*

an energy of 1275 keV is emitted in 99.9 % of the decays. However, the detected signals originating from the 1275 keV photon represent only approximately 15 % - 30 % of all events, which was verified by Geant4 simulations. Its cross section for the photoelectric

effect is way smaller than for 511 keV photons and the higher cross section of the Compton effect does not compensate this.

Figure VIII.6 shows a typical event display of a Geant4 simulation of the drilled lead converter. On the left side (xy-plane), the lead layers are clearly visible indicated by the areas holding the majority of hits. On the right side (yz-plane), the yz-position of the point like source is well distinguishable and areas without underlying lead layer indicate a noticeable decrease of hits.

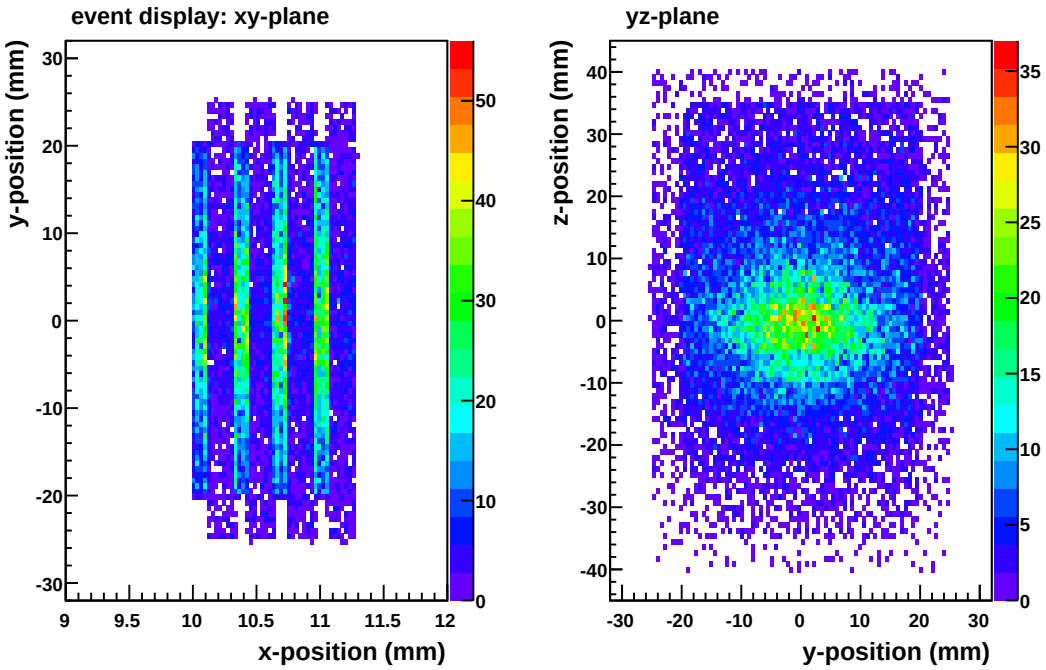

Figure VIII.6.: *A typical event display of a Geant4 simulation of the drilled lead converter. The source was positioned at a distance of 10 mm from the center of the converter.*
Left: The lead layers are indicated by the areas holding the majority of hits.
Right: The point like source is well distinguishable.

The analysis of the simulated event display gives the expected count rate. Table VIII.1 holds the expected values for the bronze and lead converters of figure VIII.3 with applied voltage and without applied voltage on the converters. Additionally, a single lead layer of 55 µm on a kapton foil of 140 µm was simulated since this was used to setup the converter test device and evaluate the first signals. For all simulations, the source was positioned at a distance of 10 mm from the converter.

Table VIII.1.: *Expectations on the count rate for different converters.*

type of converter	expected rate (Hz)
bronze	714.87 ± 18.33
lead	1078.56 ± 10.07
bronze (no voltage)	176.72 ± 9.11
lead (no voltage)	244.12 ± 4.79
singe lead layer	179.07 ± 4.10

VIII.3.3. Comparison between expectation and experiment

The single lead layer converter has been attached to the mount at a distance of 3 mm from the wire plane. The ^{22}Na- source was then positioned at a distance of (10 - 15) mm in front of the converter. Unfortunately, the exact position of 10 mm was rather hard to realize. Therefore, additional simulations of the single lead converter for varying distances of the source were implemented. The result is shown in figure VIII.7.

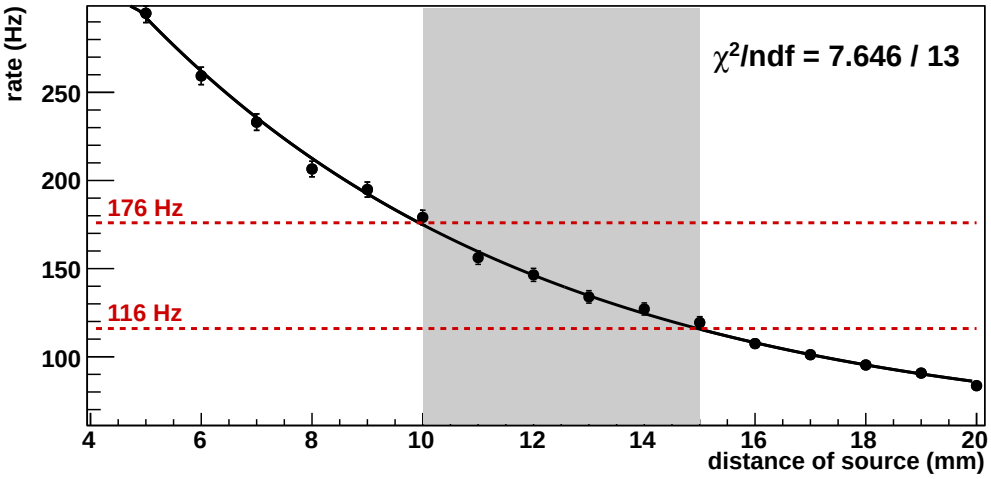

Figure VIII.7.: *Variation of the distance of the ^{22}Na- source's position showing the expected rates. The distance interval [10 mm,15 mm] corresponds to an expected rate between 116 Hz to 176 Hz.*

The rate as a function of the distance has the expected exponential behavior. The distance interval of [10 mm,15 mm] corresponds to a rate between 116 Hz and 176 Hz. The measured count rate as a function of the applied voltage is shown in figure VIII.8. At a flow of 10 l/h (black markers), a maximal count rate of 90 Hz is measured when a voltage of 2000 V is applied. The same accounts for half of the flow (5 l/h, blue markers)

which eliminates this parameter of affecting the measurements. Again, it is important that the triggering is on the right channel, otherwise a decrease in rate is observed (gray markers).

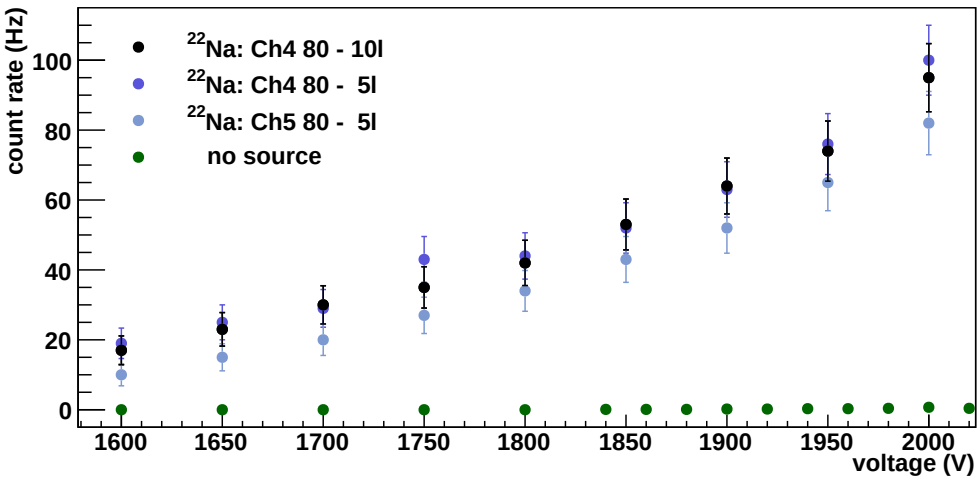

Figure VIII.8.: *The count rate is shown as a function of the applied voltage for measurements with a ^{22}Na-source in front of a single lead layer converter. The gas flow and the triggering channel were varied to estimate their affect on the count rate. As a reference, the count rates without source are plotted as well.*

The maximal count rate of (100 ± 10) Hz at 2000 V does not quite match the expected rate of (116 Hz,176 Hz). However, the expected rate is actually an upper limit and can only be reached if each created electron will also be detected, which is commonly not the case in an experimental setup. This can, for instance, be due to dead times of the electronics or avalanche signals not activating the trigger. A further affecting parameter is the activity of the source. The actual activity might be lower than declared because the last calibration is older than two years.
Since the measured count rates have the right order of magnitude, the quality of the detection property of the converter test device is stated to be satisfying, but additional evaluations considering a concrete analysis of the signals should in future be taken into account.

VIII.3.4. Energy resolution

To get an idea of the resolution properties of the converter test device and to define the optimal voltage range, an analysis of the integrated signals of a ^{55}Fe-source is necessary.

The spectrum is shown in figure VIII.9 after corrected with an analysis implemented by [Ber11]. The corrections include baseline subtraction, overflow exclusion, a time filter to set a certain time window based on the time binning of the SPADIC, and a noise filter subtracting timebin-wise the average value of all channels without signal.
The ^{55}Fe- source has an activity of 10 MBq. Its most intense X-ray emission has an energy of 5.9 keV [NNDC]. This K_α- line can be seen in figure VIII.9. Additionally, the K_α- escape peak, 2.97 eV[3] below the K_α-line, is visible. By fitting the spectrum with a Gaussian, the energy resolution can be determined to (18.00 ± 0.12) %.

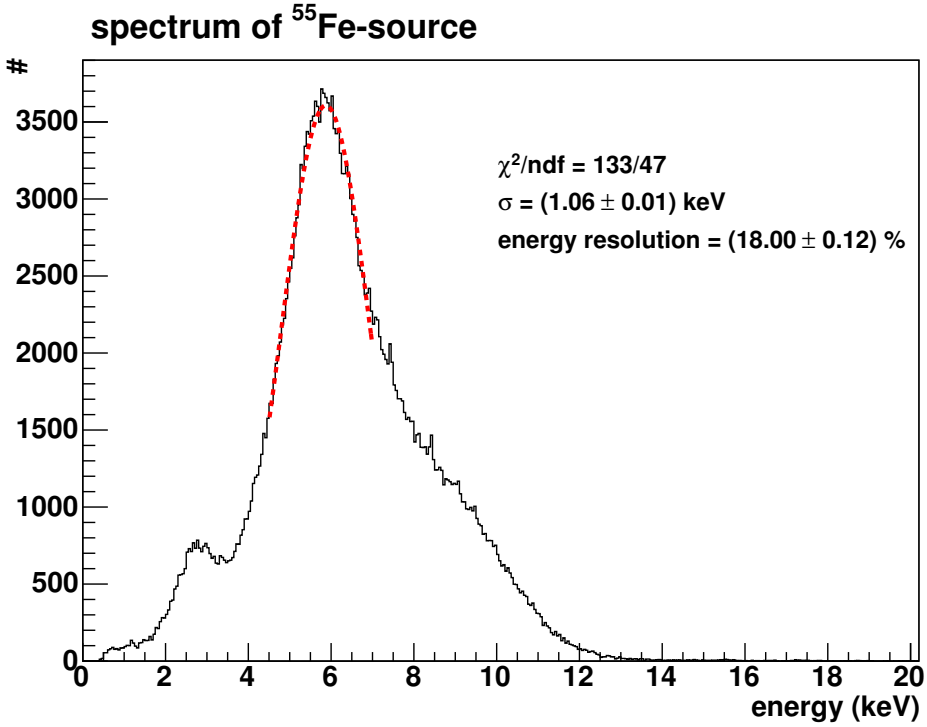

Figure VIII.9.: *Spectrum of a ^{55}Fe- source with an activity of 10 MBq measured at a voltage of 2210 V and a trigger threshold of 80 ADC values on channel 4. The K_α-line and its escape peak are clearly visible. The energy resolution could be determined to (18.00 ± 0.12) %.*

Since the dominant process for 5.9 keV photons in lead is the photoelectric effect, it is most likely to obtain 5.9 keV electrons, which are responsible for the ionization in the gas. Considering the absorption coefficient given in table VIII.2, nearly 100 % of the photons will be converted into electrons within the 55 µm lead layer. The mass stopping

[3] absorption edge of argon [Kno00]

power for 5.9 keV electrons is so high that such an electron will lose its entire energy within the following 6 mm of gas, most likely due to collisions with the argon atoms. Since the ionization energy of argon is 26 eV, the obtained signal will approximately be based on 227 primary ionized electrons.
Since the 511 keV signal will be based on only a fourth of the amount of secondary ionized electrons (see table VIII.2), the 511 keV peak is shifted left on the axis of abscissae. In the case of the ^{22}Na spectrum in figure VIII.10, the peak is then not visible, but covered by noise. Because the Compton effect and the photoelectric effect are of equal value for 511 keV and the Compton effect is even favored for photon energies of 1025 keV, the ^{22}Na spectrum shows a broad distribution.

Table VIII.2.: *Parameters to calculate the number of primary ionized electrons.*

material properties [PPB10]		
density (Pb)	$11.350\,\mathrm{g/cm^3}$	
density (Ar)	$1.66 \times 10^{-3}\,\mathrm{g/cm^3}$	
ionization energy (Ar)	26 eV	
energy dependencies [NIST]		
photon energy	5.9 keV	511 keV
mass absorption coefficient	$486.8\,\mathrm{cm^2/g}$	$0.1613\,\mathrm{cm^2/g}$
mass stopping power	$21.9\,\mathrm{MeV\,cm^2/g}$	$1.497\,\mathrm{MeV\,cm^2/g}$
number of electrons	227	57

VIII.3.5. Gain simulations

Considering several ^{55}Fe spectra for various applied voltages, the optimal voltage of operation has been determined to 1950 V. Garfield simulations of the converter test device dimensions predict thereupon a gain of 6220 for a common gas mixture of 90 % argon and 10 % CO_2. The gains for various voltages are shown in figure VIII.11. If the amount of quencher is increased (to 16 %), which can be caused by outgassing, the gain drops to 4070, which is only 2/3 and will result in remarkably smaller signals.

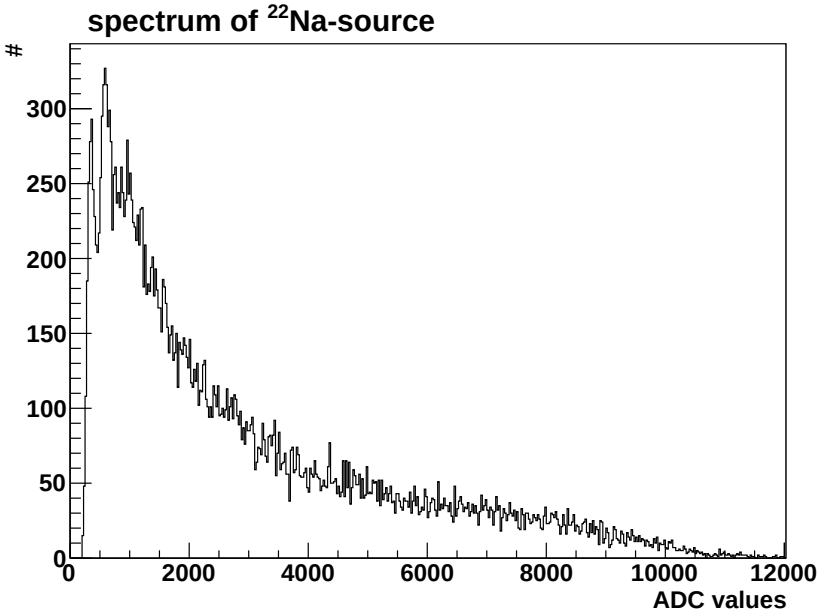

Figure VIII.10.: *Measured spectrum of the ^{22}Na-source at 2000 V and a trigger threshold of 80 ADC values showing a broad distribution caused by the Compton effect.*

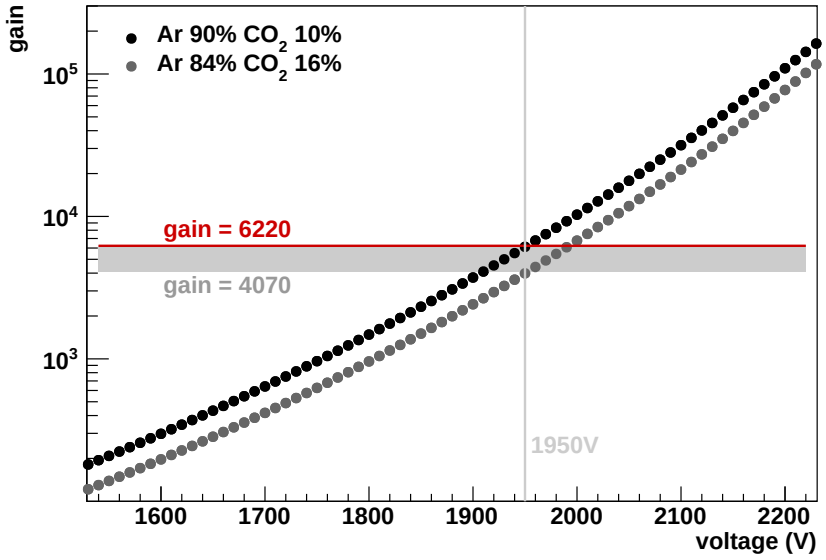

Figure VIII.11.: *Simulations of the gain dependence on the voltage for the converter test device. For a gas mixture of 90 % argon and 10 % CO_2, the gain is 6220. Increasing the quencher to 16 %, the gain drops to 2/3.*

VIII.4. Conclusion and Outlook

The design and the commissioning of the converter test device are now accomplished and the obtained count rates of the test measurements are in the range of the simulations. So far, spectra of ^{55}Fe and ^{22}Na have been collected determining an energy resolution of $(18.00 \pm 0.12)\,\%$. These are good conditions to start the test stage for the available prototype converters. Additionally, an analysis in progress should be able to correct the acquired data and estimate the quality of the prototype converters.

Summary

This diploma thesis focused on three different aspects.
At first, Geant4 simulations were implemented to examine the predictions for the sensitivity of the quadHIDAC by optimizing the converter geometry. It was found that the detection sensitivity increases strongly for converter geometries with triangular arranged holes of small ($< 400\,\mu m$) diameters and can reach values of over 20 % at a hole diameter of 100 µm. Additionally, a thicker ($> 140\,\mu m$) kapton foil as insulation layer will provide additional gain in the sensitivity, in the order of 0.5 % to 3.0 % depending on the geometry, because more electrons reach the holes and less are absorbed in the following lead layer. However, whether these numbers can be realized in practice needs further investigations since the multiplication process of the electrons inside the holes is not completely understood.
Second, a stand-alone read out method for quadHIDAC modules outside of the scanner environment was developed. It allowed to evaluate single modules before and after repair and prior to re-installation to the PET scanner. The results of chapter VII conclude that the setup installed in the PET-laboratory of the institute for nuclear physics Muenster in combination with the programmed read out code are reliably working. The developed analysis is ROOT-based and able to evaluate the general repair of a module. In the past, quadHIDAC modules have already been successfully repaired, tested, and re-installed. This work will be continued within the project B6 of the Sonderforschungsbereich 656 "Molecular Cardiovascular Imaging".
The third part of this thesis was devoted to the development and commissioning of the converter test device to evaluate the operation of prototype converters. First voltage tests were successfully accomplished, and the measured count rates show an acceptable agreement with the expectations based on Geant4 simulations. For the evaluation of energy resolution, additional measurements with a ^{55}Fe- source have been performed determining a resolution of (18.00 ± 0.12) %. In conclusion, the commissioning phase of

the converter test device can be considered a success, up to this point, and is awaiting the first measurements with test converters.

Zusammenfassung

In dieser Diplomarbeit wurden insgesamt drei Aufgabenbereiche bearbeitet.
Zunächst wurden Geant4 Simulationen implementiert um Voraussagen über das Sensitivitätsverhalten des quadHIDACs für optimierte Geometrien des Konverters zu machen. Hierbei wurde festgestellt, dass die Sensitivität steigt, wenn die Konverter eine dreischenkelige Matrixstruktur der Löcher aufweisen und zudem kleinere Durchmesser ($< 400\,\mu m$) als die Originalkonverter des quadHIDACs haben. Bei Lochdurchmessern von $100\,\mu m$ ist es möglich Sensitivitäten von über $20\,\%$ zu erreichen. In Abhängigkeit von der Lochgeometrie können zusätzliche $0{,}5\,\%$ bis $3{,}0\,\%$ an Sensitivität erreicht werden, wenn die Isolationsschicht verbreitert wird ($> 140\,\mu m$). Durch die breitere Schicht können mehr Elektronen in die Löcher gelangen und es werden weniger von ihnen in der folgenden Bleischicht absorbiert. Um diese Angaben zu überprüfen sollten im Weiteren Erkenntnisse im Bezug auf den Vervielfachungsprozess der Elektronen im Loch hinzugezogen werden, da dieser noch nicht vollständig verstanden ist.
Der zweite Schwerpunkt dieser Arbeit war die Entwicklung einer eigenständigen Auslesemethode für quadHIDAC Module, die sich außerhalb der Scannerumgebung befinden. Diese ermöglicht es einzelne Module vor und nach der Reparatur sowie vor einem Wiedereinbau in den PET-Scanner zu testen und zu beurteilen. Die Ergebnisse zeigen, dass der Test-Aufbau im PET-Labor des Instituts für Kernphysik in Münster zusammen mit dem entwickelten Auslesecode zuverlässig und betriebssicher ist. Der ROOT-basierte Auslesecode enthält eine Analyse, die es generell ermöglicht Reparaturen zu beurteilen. In der Vergangenheit wurden quadHIDAC Module bereits erfolgreich repariert und wieder in Betrieb genommen. In Zukunft wird diese Arbeit innerhalb des Projektes B6 des Sonderforschungsbereich 656 "Molecular Cardiovascular Imaging" fortgeführt.
Im letzten Teil dieser Arbeit wird die Entwicklung und Inbetriebnahme des Konverter-Teststands vorgestellt, mit dem die Funktionsweise von Prototyp-Konvertern beurteilt werden kann. Die ersten Spannungstests am Teststand wurden erfolgreich durchgeführt

und die gemessenen Zählraten stimmen mit den erwarteten Zählraten der Geant4 Simulation relativ gut überein. Um das Auflösungsvermögen des Teststands zu bestimmen wurden Messungen mit einer ^{55}Fe- Quelle gemacht, durch die eine Energieauflösung von $(18{,}00 \pm 0{,}12)\,\%$ ermittelt werden konnte. Insgesamt war die Inbetriebnahme des Konverter-Teststands bis jetzt erfolgreich und erste Messungen mit den Test-Konvertern können angegangen werden.

List of Figures

List of Tables

Bibliography

[All69] O. Allkofer. *Spark Chambers*. Thiemig, 1969.

[Arm10] T. Armbruster, P. Fischer, I. Peric. *SPADIC - A Self-Triggered Pulse Amplification and Digitization ASIC*. NSS Conference Record, 2010 IEEE, Knoxville, USA, November 2010

[Bau05] C. Baumann. *X-ray Transmission of Radiators for the ALICE-TRD*. Diplomarbeit, Institut fuer Kernphysik, WWU Muenster, 2005.

[Ber11] C. Bergmann. *private communications*. Muenster, 2011.

[Bet08] K. Bethge, G. Walter, B. Wiedemann. *Kernphysik* . Springer, 2008.

[Blu08] W. Blum, W. Riegler, L. Rolandi. *Particle Detection with Drift Chambers*. Springer, 2008.

[Bol10] K. Bolwin. *Aufbau eines Teststandes zur Evaluierung von Vieldraht-Proportionalkammern einer quadHIDAC PET Kamera in Hinsicht auf Alterung und Wiederherstellung*. European Institut of Molecular Imaging. FH Muenster, 2010

[Bro59] S. Brown. *Basic data of plasma physics*. MIT Press, 1959.

[Cha72] G. Charpak. *Filet a particules*. Decouvertes, 1972.

[Cha93] G. Charpak. *Electronic imaging of ionizing radiation with limited avalanches in gases*. Review of Modern Physics, 1993. Geneva

[Cow56] C.L. Cowan Jr., F. Reines. *Detection of the free neutrino: a confirmation.* SCIENCE Vol.124(3212), 1956.

[Dav68] C.M. Davisson. *Interaction of Gamma Radiation with Matter, Alpha-, Beta- and Gamma Ray Spectroscopy.* North-Holland Publ. Co., 1968. Amsterdam

[End81] I. Endo et al. *Systematic shifts of evaluated charge centroid for the cathode read-out MWPC.* Nuclear Instruments and Methods. North-Holland Publ. Co., 1981.

[Gat79] E. Gatti. *Optimun geometry for strip cathodes or grids in MWPC for avalanche localization along the anode wires.* Nuclear Instruments and Methods. North-Holland Publ. Co., 1979.

[Got10] H. Gottschlag. *Small Animal Positron Emission Tomography with Multi-Wire Proportional Counters.* Dissertation, Institut fuer Kernphysik, WWU Muenster, 2010.

[J+99] A. Jeavons et al. *A 3D HIDAC-PET Camera with Sub-millimetre Resolution for Imaging Small Animals.* IEEE Trans. Nucl. Sci. 46 3.

[Jea95] A. Jeavons. *Radiographic detector with perforated cathode*, 1995. US Patent 5,434,468.

[Jea02] A. Jeavons. *Imaging system using a high-density avalanche chamber converter*, 2002. US Patent 6,404,114.

[Kle92] K. Kleinknecht. *Detektoren fuer Teilchenstrahlung.* Teubner, 1992.

[Kno00] G.F. Knoll. *Radiation Detection and Measurements.* John Wiley & Sons, 2000.

[Kor46] S.A. Korff. *Electron and Nuclear Counters-Theory and Use.* Van Nostrand Company, 1946.

[Leo87] W. Leo. *Techniques for Nuclear and Particle Physics Experiments.* Springer, 1987.

[Mat84] E. Mathieson. *Cathode Charge Distribution in Mulitwire Chambers.* Nuclear Instruments and Methods. North-Holland Publ. Co., 1984.

[Mat88] E. Mathieson. Nucl. Instr. and Meth. 270 (1988) 602.

[Mel66] A. Melissinos. *Experiments in Modern Physics*. Academic Press, New York, 1966.

[NIST] National Institute of Standards and Technology. *Physical Reference Data*. Gaithersburg, 11/30/2011. `http://physics.nist.gov/`.

[NNDC] National Nuclear Data Center. *Database: Nuclear Structure and Decay Data*. Brookhaven National Laboratory, 11/20/2011. `http://www.nndc.bnl.gov/`.

[Nol89] W. Nolting. Grundkurs Theoretische Physik 3 Elektrodynamik . Vieweg, 1989.

[Phe06] M.E. Phelps. *PET: Physics, Instrumentation, and Scanners*. Springer, 2006.

[Pie08] J.-F. Pietschmann. Institut fuer Kernphysik, WWU Muenster, 2008.

[Pov04] B. Povh, K. Rith, C. Scholz, F. Zetsche. *Teilchen und Kerne*. Springer, 2004.

[PPB10] K. Nakamura et al (Particle Data Group). *Particle Physics Booklet*. Review of Particle Physics. California, July 2010.

[Sau77] F. Sauli and CERN. Geneva. *Principles of operation of multiwire proportional and drift chambers*. Imprint 3 (1977) 92

[Sch05] K.P. Schäfers et al. *Performance Evaluation of the 32-module quadHIDAC Small-Animal PET Scanner*. J. Nucl. Med. 46 6 (2005) 996.

[Tow06] D.W. Townsend, D.L. Bailey, P.E. Valk, M.N. Maisey. *Positron Emission Tomography*. Springer, 2006.

[Ver10] D. Vernekohl. *Measurements with a Multi-Wire Proportional Chamber for Small Animal Positron Emission Tomography*. Diplomarbeit, Institut fuer Kernphysik, WWU Muenster, 2010.

[Ver11] D. Vernekohl. *private communications*. Muenster, 2011.

[Wer04] M.N. Wernick, J.N. Aarsvold. *Emission Tomography - The fundamentals of PET and SPECT*. Elsevier Inc., 2004.

Eigenständigkeitserklärung

Hiermit versichere ich, dass ich die vorliegende Arbeit selbständig verfasst und keine anderen als die angegebenen Hilfsmittel benutzt habe. Die Stellen der Arbeit, die dem Wortlaut oder dem Sinn nach anderen Werken entnommen sind, wurden unter Angabe der Quelle kenntlich gemacht.

Münster, 15. Dezember 2011

Jennifer Bersch

Danksagung

Am Ende möchte ich mich noch bei allen bedanken, die mich in den letzten Jahren unterstützt und zum Gelingen dieser Arbeit beigetragen haben.

Herrn Prof. Dr. Johannes P. Wessels danke ich für die Möglichkeit diese Arbeit in seiner Arbeitsgruppe im Projekt Small Animal PET anzufertigen.
Allen, die in dem Projekt Small Animal PET tätig sind, danke ich für die Hilfe, Kritik, Diskussionen und Ideen, die meine Arbeit unterstützt haben. Dieses gilt vor allem für Björn, Don, Klaus und Konstantin.
Dr. Christian Klein-Bösing, PD Dr. Klaus Schäfers und Don Vernekohl danke ich insbesondere für die kritische Durchsicht meiner Arbeit und viele nützliche Tipps.
Den Mitgliedern der AG Wessels und des Instituts für Kernphysik danke ich für eine gute Arbeitsatmosphäre und weitgehende Hilfestellung bei jeder Art von Problemen.
Auch den Mitgliedern von E-Werkstatt und Feinmechanischer Werkstatt, die viel zu dieser Arbeit beigetragen haben, möchte ich hier noch einmal ausdrücklich danken. Das gilt besonders für Norbert Heine, der viele technische Probleme zu lösen wusste.

Ganz besonders möchte ich mich hier bei all denen bedanken, die einen besonderen Platz in meinem Leben einnehmen.

Pia, Florian, Hans und Rike danke ich für die vielen schönen Stunden während des gesamten Studiums.
A special thanks goes to Ethan and Cecilia for all their help, especially regarding style of speech, but also for the lovely Italian pasta, which saved some of my days.
Esco, Jonas, Tine, Nina, Anna, Sven. Vielen Dank für all die lustigen Abende, guten Tipps und das Zuhören! Ohne diese Ablenkungen wäre ich sicher das ein oder andere Mal auf der Strecke geblieben. Auch Vroni und Martin haben hier ihren Teil dazu

beigetragen. Liebe Esco, ich werde ganz besonders deine gute Küche vermissen.
Kathi, und Peter: Dank u wel! Es ist gut eine beste Freundin wie dich zu haben.
Änne, Veronika, Hans und Friederike danke ich für jegliche Unterstützung innerhalb der letzten Jahre. Auch wenn es nicht immer ganz einfach war, ich konnte mich immer auf euch verlassen.
Ein großer Dank geht auch an Oma, Opa, und Oma, die mir in jeder denkbaren Art und Weise zur Seite stehen, wann immer ich es brauche.
Mama und Papa, es gibt kaum Worte, die beschreiben wie dankbar ich euch bin. Danke für alles, was ihr möglich gemacht habt und eure bedingungslose Liebe.
Kevin, du bist der beste Bruder!
Schließlich möchte ich noch demjenigen danken, der mich jeden Tag von Neuem erfreut und täglich für mich da ist, wo und wie es nur irgendwie geht. Unsere Erfahrungen und Erlebnisse sind gegen nichts in dieser Welt einzutauschen. Danke, Johannes!